

1 **Investigation on the influence of antimony tin oxide/silver nanofluid on direct**
2 **absorption parabolic solar collector**

3 Sreehari Sreekumar^a, Albin Joseph^b, Sujith Kumar C. S^a, Shijo Thomas^{*b}

4 ^aDepartment of Mechanical Engineering, National Institute of Technology Calicut, 673601, India

5 ^bSchool of Materials Science and Engineering, National Institute of Technology Calicut, 673601,
6 India

7 Corresponding author: Shijo Thomas, Email address: shijo@nitc.ac.in

8 **Abstract**

9 This paper discusses the synthesis and characterization of a novel hybrid nanofluid and its
10 performance analysis on a parabolic trough direct absorption solar collector. Broadening the
11 absorption spectra of working fluid using nanoparticles is the new research revolution for
12 increasing the volumetric solar absorption efficiency. It is reported that plasmonic silver
13 nanoparticles have higher absorption in visible spectra while antimony doped tin oxide has an
14 absorption peak in the near-infrared region. Hence, antimony tin oxide/silver hybrid nanoparticle
15 with broad spectral absorptivity was synthesized. Optimization of the nanofluid composition
16 performed using response surface methodology yielded an optimized mass fraction of antimony
17 tin oxide and surfactant, sodium dodecyl sulfate, as 0.1% each. The solar weighted absorption
18 fraction of optimized nanofluid was obtained as 90.12%. Performance evaluation of the solar
19 collector was based on ASHRAE standards 93-2010. The optical efficiency of the parabolic
20 collector was calculated to be 75%. The maximum thermal efficiency obtained by the optimized
21 nanofluid applied parabolic trough direct absorption solar collector was 63.5% at a flow rate of
22 **0.022 kgs⁻¹** and the highest exergy efficiency obtained was 5.6%. Thermal and exergy efficiency
23 was observed to increase with increase in flow rate.

24 **Keywords:** ATO/Ag hybrid nanoparticle, solar weighted absorption fraction, optimization, direct
25 absorption, photothermal conversion.

26

27

28 Nomenclature

English Parameters

A	Aperture area [m^2]	K	Geometric factor
C_p	Specific heat [$J kg^{-1} K^{-1}$]	L_a	Receiver tube length [m]
D_{out}	Outer diameter of the receiver [m]	\dot{m}	Mass flow rate [$kg s^{-1}$]
d	Universal non-random error parameter due to receiver mislocation and reflector profile errors	s_{in}	Entropy of heat transfer fluid at inlet [$kJ kg^{-1} K^{-1}$]
f	Focal distance [m]	s_{out}	Entropy of heat transfer fluid at outlet [$kJ kg^{-1} K^{-1}$]
h_{in}	Enthalpy of heat transfer fluid at inlet [kJ]	T_{amb}	Ambient temperature [K]
h_{out}	Enthalpy of heat transfer fluid at outlet [kJ]	T_{fm}	Mean fluid temperature [K]
I	Solar intensity [$W m^{-2}$]	T_{in}	Inlet temperature of heat transfer fluid [K]
I_λ	Solar spectral intensity [$W m^{-2} nm^{-1}$]	T_{out}	Outlet temperature of heat transfer fluid [K]
		T_s	Temperature of the sun [K]
		Q_{sol}	Solar radiation intensity [W]
		W_a	Aperture width [m]

Greek Parameters

α	Absorptance	λ	Wavelength [nm]
$\alpha_{receiver}$	Absorbance of reflector	τ	Transmittance
β	Universal non-random error parameter due to angular errors	τ_{cover}	Transmittance of the cover glass
γ	Intercept factor	φ_r	Rim angle of collector [rad]
η_{ex}	Exergy efficiency	ψ	Exergy [W]
η_{th}	Thermal efficiency	ψ_{dest}	Exergy destruction rate [W]
θ	Incidence angle [rad]	ψ_{in}	Total exergy entering the system [W]
ρ	Reflectance	$\psi_{m,in}$	Exergy inflow rate by heat transfer fluid [W]
$\rho_{collector}$	Reflectance of collector sheet	$\psi_{m,out}$	Exergy inflow rate by heat transfer fluid [W]
σ	Universal random-error parameter	ψ_{out}	Total exergy exiting the system [W]
		ψ_{sol}	Solar radiation exergy absorption rate [W]

Abbreviations

ASTM	American Society for Testing and Materials	NIR	Near-infrared
ANOVA	Analysis of Variance	PTDASC	Parabolic Trough Direct Absorption Solar Collector
DOE	Design of Experiments	RSM	Response Surface Methodology
LSPR	Localized Surface Plasmon Resonance		

29

30 1. Introduction

31 Cleaner and sustainable energy technologies are gaining importance due to the increase in
32 environmental pollution and the current energy demand. Solar energy is a reliable and promising
33 one among the renewable energy resources. Researches on increasing the energy conversion
34 efficiency of solar energy systems are taking place at a burgeoning speed. Photothermal,
35 photochemical and photovoltaic conversions are the prominent methods of solar energy utilization.
36 Photothermal systems are having the highest energy conversion efficiency among the other solar
37 energy conversion techniques. Among the solar thermal systems, concentrating solar collectors are
38 having higher thermal efficiency compared to non-concentrating collectors. A typical
39 concentrating solar collector is based on three main steps: (i) concentrating the solar radiation on
40 the receiver surface, (ii) energy conversion at the absorber surface and, (iii) heat transfer from
41 absorber surface to working fluid by convection and conduction [1]. In such systems, the
42 maximum temperature is occurring at the absorber surface immersed in water due to which the
43 heat loss to the surrounding increases. They also show an increase in thermal resistance during
44 heat transfer from the absorber surface to the working fluid. Direct absorption Solar Collectors
45 (DASC) works on the principle of volumetric absorption of solar radiation. Since water and
46 thermal oils have poor optical absorption properties, nanofluids are used in DASC. The energy
47 gain of fluid by convective heat transfer from surface absorbers in a conventional solar collector
48 is transformed into radiative transfer in a participating medium (nanofluid) in DASC. Synthesizing
49 nanofluids with a higher photo-thermal conversion rate improves solar absorption efficiency. Vast
50 research on synthesis, characterization, and testing of nanofluids with high thermal conductivity
51 and optical absorptivity, like Ag, Au, carbon nanotubes (CNT), Cu, graphite, graphene, and metal
52 oxides, have been performed.

53 The concept of volumetric absorption was first proposed by Minardi et al. [2] in 1975. Tyagi
54 et al. [3] were the first to propose a theoretical model for DASC. From the theoretical analysis, the
55 direct absorption was found to have higher efficiency compared to surface absorption. Otanicar et
56 al. [4] investigated the direct absorption capability of different base fluids by comparing their
57 extinction coefficients and found water to be better than thermal oils. Photothermal conversion of
58 nanofluids synthesized using metal (Cu, Au, Ag), metal oxide (CuO, Al₂O₃, TiO₂) and nonmetal
59 (GO, MWCNT) nanoparticles were performed over the years. Chen et al. [5] studied the
60 photothermal conversion property of Au nanofluids and found that efficiency increased with an
61 increase in the volume fraction of nanoparticle. Experimental analysis on the photothermal
62 conversion property of gold nanofluids was performed by Beicker et al. [6]. Amjad et al. [7]
63 analyzed the photothermal conversion capability of different nanofluids to be used for direct
64 absorption applications. The results showed that silver nanofluid exhibited maximum energy
65 conversion efficiency. Abdelrazika et al. [8] examined the influence of water-based silver
66 nanofluid on the performance of hybrid photovoltaic-thermal collectors. Results showed that the
67 transmittance of nanofluid decreased with an increase in collector depth and nanofluid volume
68 fraction. Valizade et al. [9] performed an experimental investigation on direct absorption using
69 nanofluids and metal foams of CuO and SiC material. Nanofluid absorber exhibited enhancement
70 over its respective metal foam in the case of copper oxide. Chen et al. [10] performed photo-
71 thermal conversion investigations on cupric oxide (CuO) and antimony tin oxide (ATO) binary
72 nanofluid. ATO provided complementary optical absorption due to its better solar absorption at
73 near-infrared (NIR) spectra. Investigation performed by Yu et al. [11] concluded that the
74 dispersion stability of nanofluid is having a direct impact on optical absorptivity. **Even though the**
75 **property of base fluid could be enhanced by addition of nanoparticle, there are some limitations.**
76 **Some of the drawbacks associated with nanofluids are the higher cost, time-consuming nanofluid**
77 **synthesis process, lesser stability, and higher viscosity.**

78 A hybrid nanoparticle has an advantage over mono-component nanoparticle as it exhibits
79 synergetic properties of the multiple components present in the structure. Property tunability at
80 particle level is the advantage of hybrid nanofluid over binary nanofluid. According to the authors'
81 knowledge hybrid nanoparticles with selective spectral absorptivity are less explored. Yu et al.
82 [12] synthesized CuO/Ag composite nanoparticle for solar direct absorption application. Jiang et
83 al. [13] synthesized Ag-Ag₂S core-shell structure with broad absorption spectra which exhibited

84 an absorption peak in the wavelength range of 300 nm-1100 nm. Zeng et al. [14] synthesized
85 Sn/SiO₂/Ag core-shell PCM nanoparticle for thermal energy storage and solar absorption. Zeng et
86 al. [15] synthesized silver-based SiO₂/Ag plasmonic hybrid nanofluid and its binary nanofluid with
87 NIR absorbing MWCNT nanoparticle. Zeng et al. [16] synthesized a full spectrum absorption
88 hybrid nanoparticle. Visible spectrum absorbing TiN nanoparticle and NIR absorbing magnetic
89 Fe₃O₄ nanoparticle was selected as hybrid material components. This was one of the few papers
90 on full spectral absorption hybrid nanoparticle.

91 Design of experiments (DoE), fuzzy logic and artificial neural network (ANN) are the most
92 preferred tools for finding the interaction of input parameters on the output response. Out of these,
93 DoE will provide an insight into the dependence of response on input parameters in a minimum
94 number of experiments [17]. Esfe et al. [18] optimized the rheological and thermal properties of
95 Al₂O₃-EG/water nanofluid by using response surface methodology (RSM).

96 The advantage of a DASC is that the maximum temperature is
97 occurring within the fluid volume and hence the need for a hotter absorber tube surface can be
98 avoided. In addition, the energy efficiency of the collector could be improved by increasing the
99 solar spectral absorptivity of nanofluid by modifying the morphology, material property (thermal
100 and optical) and mass fraction of the nanomaterial. The thermo-economic analysis was conducted
101 on the performance of a DASC by Otanicar et al. [19]. The studies compared the economic and
102 environmental impact of DASC on residential water heating applications and proved that in
103 addition to 3% improvement in thermal efficiency of the collector, the DASCs are providing the
104 same economic benefit as a conventional collector. Applicability of hybrid nanofluid in
105 conventional parabolic trough collectors was extensively reviewed by Minea et al. [20]. However,
106 experimental investigations performed on DASC using hybrid nanofluids are very rare compared
107 to single and binary nanofluids. Bellos et al. [21] performed an investigation on the performance
108 of a parabolic trough collector using oil-based Al₂O₃-TiO₂ hybrid nanofluid. The analysis shows
109 that enhancement in the thermal efficiency of PTC using hybrid nanofluid was higher than the
110 mono nanofluids. Delfani et al. [22] conducted experimental and numerical analysis on the thermal
111 performance of MWCNT nanofluid based DASC for residential application and reported an
112 improvement of 10-29% in thermal efficiency, over that of the base fluid. The efficiency was found
113 to be an ascending function of volume fraction and flow rate. Vakili et al. [23] evaluated flat plate

114 DASC with graphene nanoplatelets as working fluid for domestic water heating applications. The
115 maximum thermal efficiency was obtained at an optimum mass flow rate of 0.015 kg s^{-1} . Menbari
116 et al. [24] on examining CuO as working fluid in PTDASC found that thermal efficiency of 52%
117 was achievable by varying volume fraction of the nanofluid. Menbari et al. [25] performed an
118 experimental analysis on CuO/Al₂O₃ binary nanofluid being applied in PTDASC. The thermal
119 efficiency of PTDASC having binary nanofluid was found to be 48%. Although numerous works
120 on energy analysis of DASCs has been reported, experimental works on the exergy analysis on
121 direct absorption solar collectors are very few. An extensive review of the exergy analysis of solar
122 collectors and its significance on the performance investigation was performed by Kalogirou et al.
123 [26]. Gorji and Ranjbar [27] carried out thermal exergy analysis on DASC for optimizing the
124 performance parameters of the system. Response surface methodology was used for optimizing
125 the parameters like incident solar flux, nanofluid volume fraction and flow rate. Maryam Karami
126 [28] reported an enhancement in the thermal efficiency of 21.7% for DASC with hybrid nanofluid
127 over the base fluid.

128 From the literature review, it is clearly inferred that most of the hybrid nanoparticles synthesized
129 have Ag as one of its components due to its LSPR effect. ATO is a viable option for nanoparticles
130 with NIR absorption [10]. Among the available base fluids, water is reported to be having the
131 highest optical absorptivity [4]. Investigations on hybrid nanofluids with wide spectrum solar
132 absorption in PTDASC is also very limited in the reported literature. Design of Experiments (DoE)
133 could be adopted as a useful tool for the optimization of parameters based on output response with
134 a minimal number of experiments.

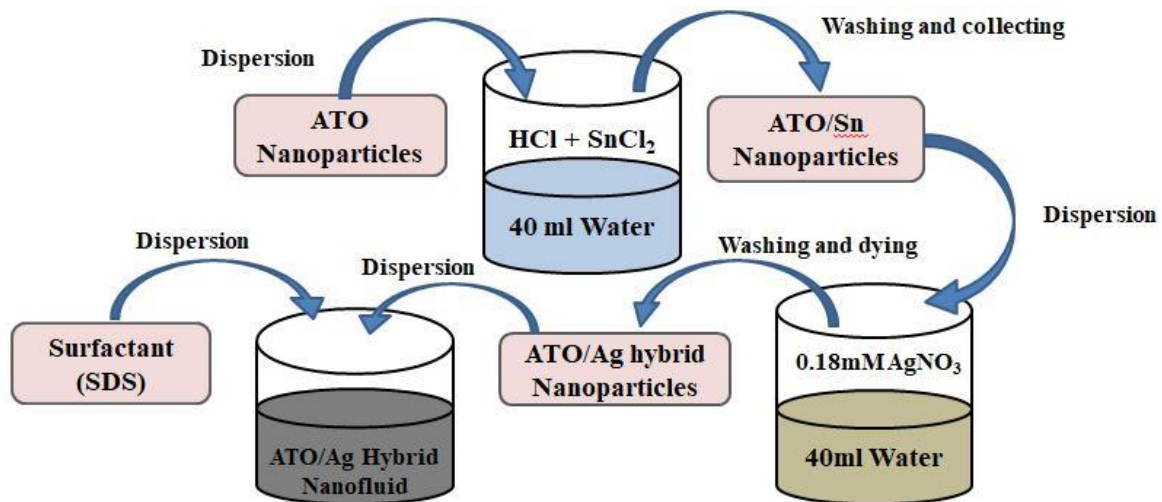
135 In this work, synthesis, characterization, and optimization of a novel ATO/Ag hybrid
136 nanoparticle having broad spectral absorption property are performed. Based on the design of
137 experiments concept a design matrix was created with different mass fractions of components
138 based on which the synthesis and characterization of nanofluids were performed. Response surface
139 methodology was adopted for finding the effect of nanoparticle and surfactant mass fractions on
140 the solar weighted absorption fraction of nanofluid. The optimized mass fraction and surfactant
141 concentration were calculated using the desirability function in 'Design Expert' software.
142 Parametric study was also performed to analyze the effect of mass fraction of nanoparticle and the

143 penetration depth of light on optical absorptivity. Experimental investigations were conducted on
144 optimized hybrid nanofluid based PTDASC and, energy and exergy analysis were performed.

145 2. Synthesis and characterization of hybrid nanoparticle

146 2.1. Synthesis of ATO/Ag hybrid nanoparticle

147 ATO nanoparticle was supplied by Sigma Aldrich. The hybrid nanoparticle is synthesized using
148 facile one-step reduction reaction [15, 29] using Sb_2O_5 , SnCl_2 , HCl , AgNO_3 and ATO
149 nanoparticles (Sigma Aldrich). The ATO nanoparticles are dispersed in a medium of pH greater
150 than its isoelectric point (IEP). The IEP of tin oxide is in a range of +2 and +4 while the IEP of
151 Sb_2O_5 lies between +3 and +5 [30]. IEP of ATO lies in between the constituents. Hence the
152 particles will gain a negative charge on dispersion in base fluid [15]. 200 g of SnCl_2 and 300 μl of
153 HCl are mixed in 40 ml of DI water, and then ATO nanoparticles are dispersed in this medium.
154 The pH of the reaction environment is adjusted by rinsing in water continuously. pH is set to 7 for
155 further reaction process. ATO surface will have a negative charge in this reaction environment.
156 ATO nanoparticle is activated with Sn^{2+} by inorganic grafting between OH^- groups on the surface
157 [29]. AgNO_3 solution of 40ml is prepared and mixed with the above solution. $\text{ATO}/\text{Sn}^{2+}$ wet
158 mixture on reaction with silver nitrate solution undergoes a reduction process to produce Ag^+ ions
159 in solution. The charge difference is the potential for Ag deposition on the surface of ATO [29].
160 Finally, the deposited ATO/Ag nanoparticle is washed and dried in a hot air oven maintained at
161 60°C . The synthesis process is graphically represented in Fig.1.



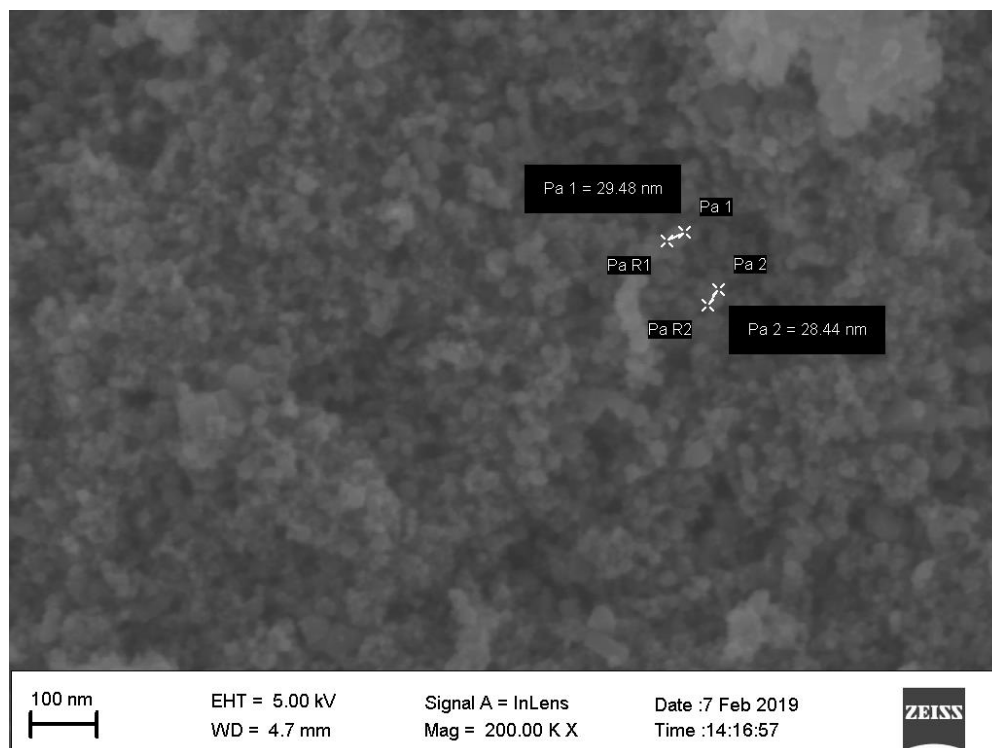
162

163 **Fig. 1.** Methodology used in the synthesis of ATO/Ag nanoparticle and nanofluid

164 2.2. Morphological characterization

165 Morphological characterization of nanoparticle was done using high-resolution transmission
166 electron microscopy (Jeol/JEM 2100) and scanning electron microscopy (Zeiss HV SIGMA
167 FESEM). Morphological analysis carried out using the SEM image given by Fig. 2 shows that the
168 ATO nanoparticles are not fully spherical. The size of ATO/Ag nanoparticles is varying in the
169 range of 20 – 50 nm. As observed in Fig. 2, it is obvious that the size of the Ag nanoparticle is less
170 than 10 nm. The SEM image of ATO/Ag hybrid nanoparticles is seen to be in a clustered form due
171 to its smaller size. The TEM image of hybrid nanoparticle as displayed in Fig. 3 confirms the
172 deposition of Ag on the surface of ATO nanoparticle. SEM image is unable to show the
173 crosslinking between the particles as the size of particles falls below 40nm and the shape of
174 particles is not spherical. Hence the SEM-EDAX is performed to show the presence of silver
175 particles in the as-prepared particle sample.

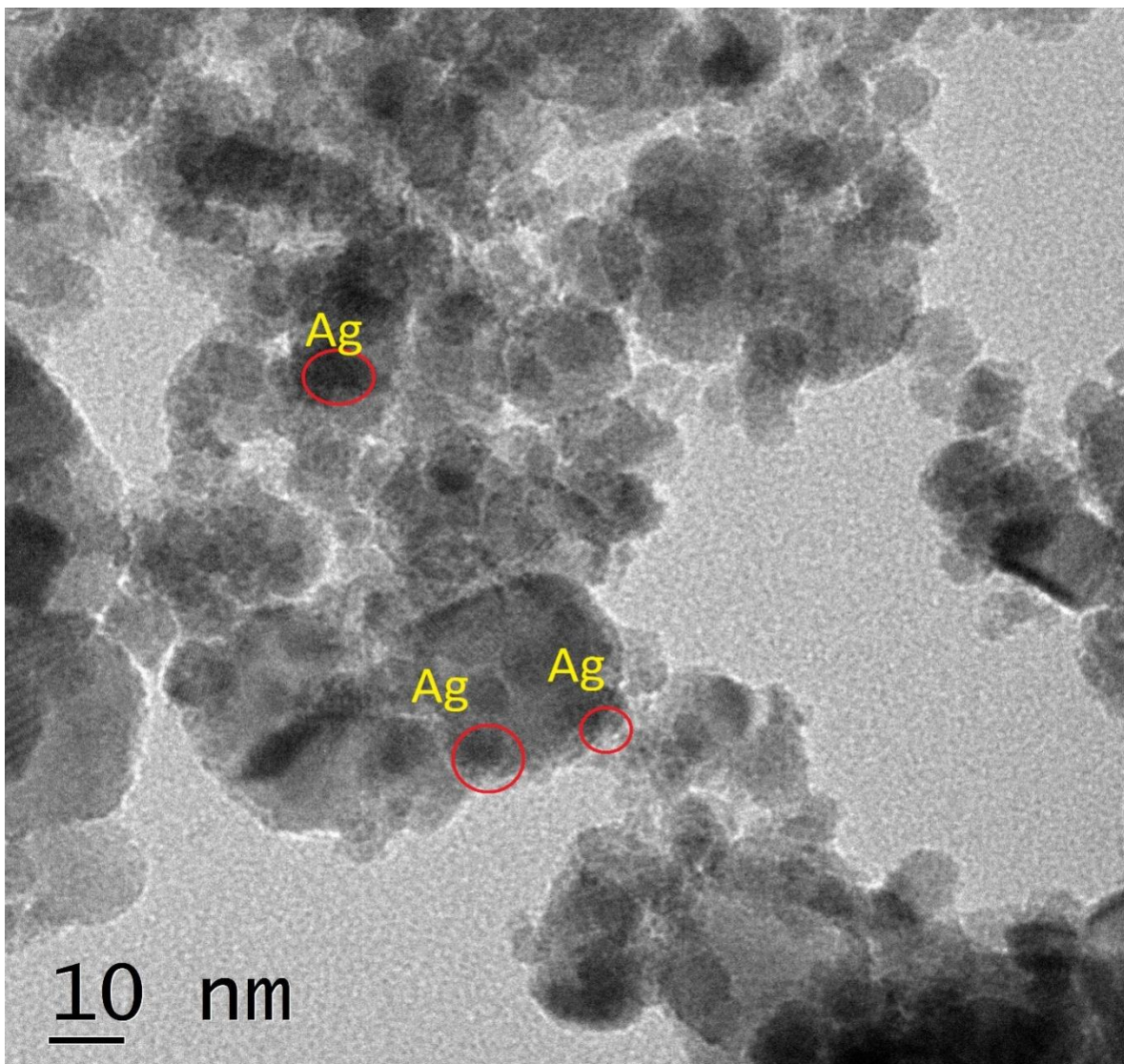
176



177

178

Fig. 2. SEM images of ATO/Ag hybrid nanoparticle



179

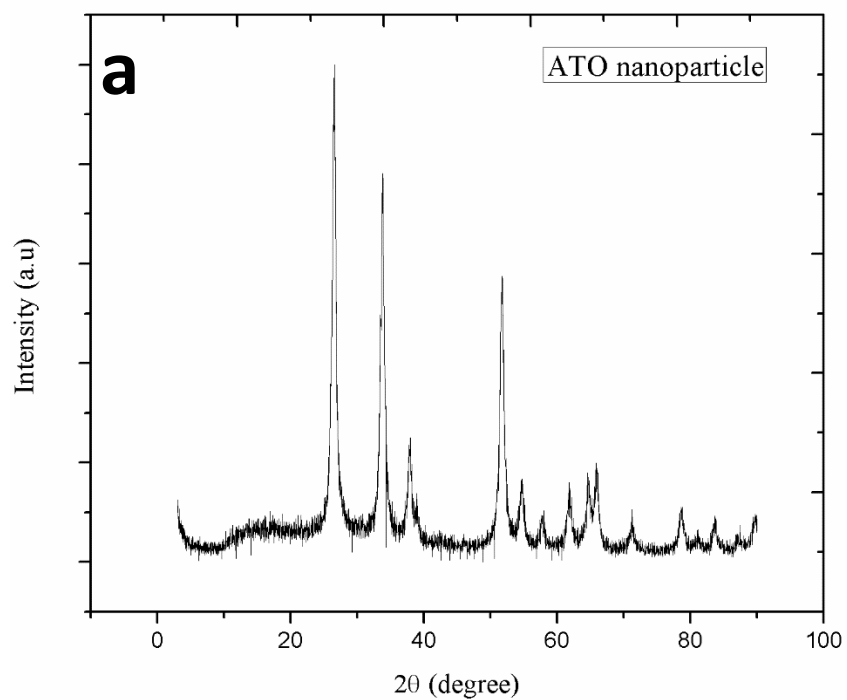
180

Fig. 3. TEM image of ATO/Ag hybrid nanoparticle

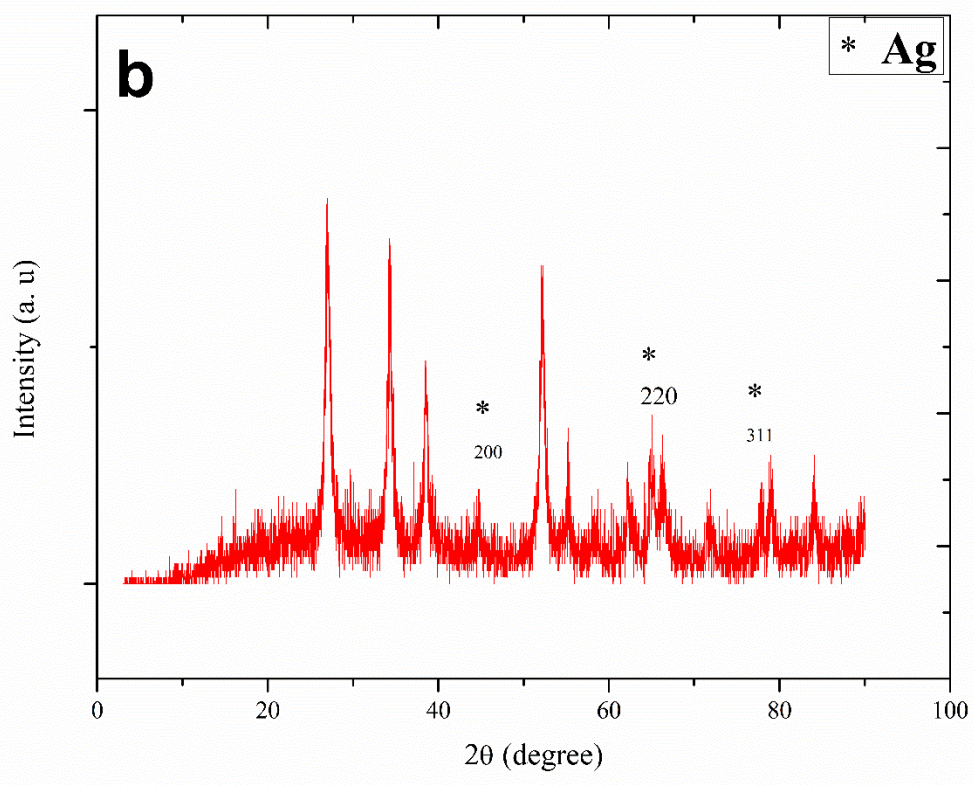
181 *2.3. Phase structure analysis of hybrid nanoparticle*

182

183 The XRD spectrum of ATO/Ag hybrid nanoparticle and ATO nanoparticles are shown in Fig 4.
184 ATO nanoparticle is having tetragonal rutile structure. The major peaks of ATO nanoparticle
185 corresponding to (100), (101), (200) and (211) crystallographic planes (JCPDS 88-0287) were
186 observed in the XRD analysis. The peaks of Ag nanoparticle (JCPDS 04-0783) with FCC structure
187 confirm the presence of Ag. FCC structured silver nanoparticle is having peaks that are indexed to
188 its (111), (200), (220) and (311) crystallographic planes.



189



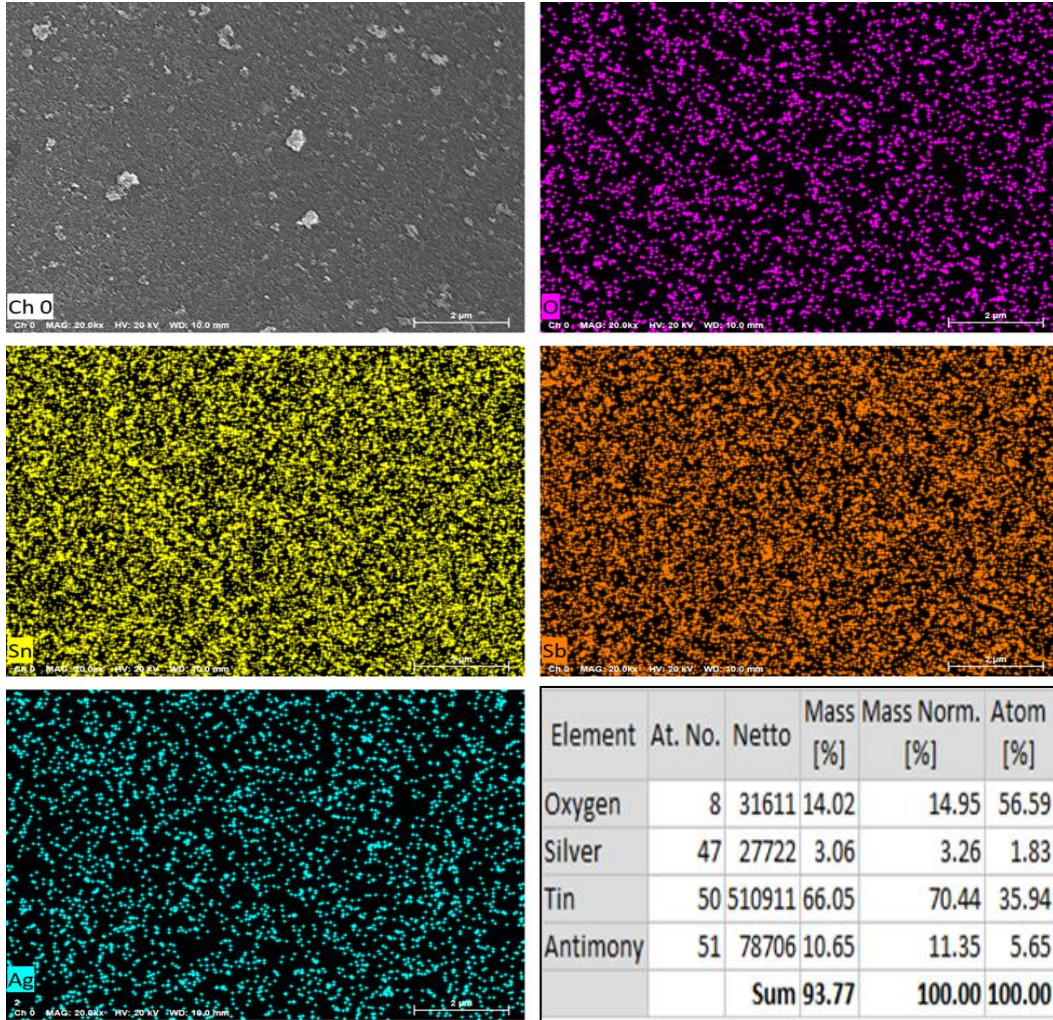
190

191

Fig. 4. XRD spectrum of (a) ATO nanoparticle, (b) ATO/Ag hybrid nanoparticle

192 2.4. *Composition analysis of hybrid nanoparticle*

193 Energy-Dispersive X-ray (EDAX) spectroscopic analysis is used to perform the elemental
194 mapping of constituent elements present in a material. The composition of different elements of
195 the synthesized hybrid nanomaterial was found by analyzing the X-rays emitted after bombarding
196 with the electron beam from the test sample. Fig. 5 depicts the elemental distribution and
197 composition in the ATO/Ag hybrid nanomaterial sample. The EDX spectroscopic results, as
198 observed from Fig. 5, can also be used to confirm the presence of proposed elements in the hybrid
199 material. The presence of ATO nanoparticle is confirmed by the occurrence of its main elements,
200 Sn and Sb, which are having the maximum mass fractions of 66% and 10%. Ag which has 3% of
201 mass fraction in the hybrid nanoparticle sample is also uniformly distributed in the sample, as
202 observed from the mapping. As the size of the silver nanoparticle is almost half of ATO, the silver
203 content in the area is less as observed from the mapping. From Fig. 5, it is inferred that the hybrid
204 nanoparticles of the required components are synthesized, and have an even distribution of
205 particles in the prepared sample.



206

207 **Fig. 5:** FESEM-EDAX mapping of ATO/Ag hybrid nanoparticle and composition table

208 **3. Synthesis and characterization of Nanofluid**

209 *3.1. Preparation of nanofluid*

210 The ATO/Ag hybrid nanoparticle is dispersed in DI water at the required mass fractions. For
 211 improving the stability of the prepared nanofluid, Sodium Dodecyl Sulfate (SDS) is added as
 212 surfactant. The addition of SDS as a surfactant produces surface charge on the particle which
 213 prevents the agglomeration of nanoparticles, thereby providing a highly stable and fully dispersed
 214 nanofluid. The surfactant-induced electrostatic dispersion stability is due to reduced inter-particle
 215 interaction [11].

216 Reducing the number of experiments to arrive at the optimum composition of ATO, Ag,
217 and SDS is required to minimize the usage and waste of various chemicals. For obtaining the
218 optimum composition that yields maximum optical absorption, response surface methodology
219 (RSM) in Design Expert 10 was employed. RSM provides a clear insight of input variables
220 interaction on output response using a minimum number of experimental runs [17]. The parameters
221 considered for optimization are the concentrations of nanoparticle and surfactant. The mass
222 fraction was varied from 0.01 to 0.2 % for ATO/Ag nanoparticle and 0.1 to 0.2% for SDS. The
223 maximum limit of SDS concentration is selected so that the Critical Michelle Concentration
224 (CMC) point is not reached. The maximum concentration of nanoparticles was selected based on
225 the literature survey on the same individual nanoparticles. An increase in concentration was
226 reported to increase the thermal conductivity but favors agglomeration. Hence the range that was
227 reported in the literature to provide maximum absorption was taken as the limits of nanoparticles
228 in the design matrix to find the optimum concentration. Stability analysis of the colloidal solution
229 was performed for the mono-component ATO nanofluid, ATO/Ag hybrid nanofluid with
230 optimized mass fraction and, ATO/Ag hybrid nanofluid with the maximum concentration of
231 ATO/Ag from the design matrix as described in section 5.4.

232 According to the design matrix given in Table 1, different combinations of ATO, Ag, and
233 SDS are subjected to spectroscopic analysis. Nine different combinations of constituent mass
234 fractions and four same combinations of component mass fractions are presented in Table 1. A
235 combination which is the mean of high and low levels is repeating four times in the design matrix.
236 The reproducibility of the results is verified by cross-checking with the results obtained for
237 repeated combinations. The response parameter based on which the optimized combination is
238 arrived at is the solar weighted absorption fraction.

239

240

241

242

243

244

Table 1: Design matrix for preparing nanofluids with combinations of mass fraction

Run	Input Variables	
	ATO/Ag (% mass fraction)	SDS (% mass fraction)
1	0.01	0.15
2	0.11	0.15
3	0.11	0.1
4	0.11	0.15
5	0.11	0.15
6	0.04	0.11
7	0.17	0.19
8	0.11	0.2
9	0.04	0.19
10	0.17	0.11
11	0.2	0.15
12	0.11	0.15
13	0.11	0.15

245

246 *3.2. Thermal conductivity*

247 The thermal conductivity of the samples was measured with the KD2 Pro Thermal Property Meter
248 (Decagon Devices). The KD2 Pro uses a transient line heat source method to obtain the transient
249 temperature profile of fluid which is then compared with the full exponential integral solution of
250 the heat equation to obtain the thermal conductivity. The measurements are done at a constant
251 temperature of 29.5 °C for all samples. Three sets of readings were made for each sample and the
252 average is taken as given in Table 2. The results reveal that the thermal conductivity of hybrid
253 nanofluid samples is not a linear function of the concentration of nanoparticle and surfactant.
254 Thermal conductivity values are given in Table 2.

255

256 3.3. *Optical property characterization*

257 UV-Vis spectrophotometer (SHIMADZU) with a spectral range of 280nm-1200nm is used for the
 258 optical characterization of the nanofluids. The wavelength range is sufficient in analyzing the
 259 optical absorptivity of broad-band spectral absorbing nanofluids as the complete extinction of
 260 radiation takes place in this spectral range [13, 31].

261

262 **Table 2: Thermal conductivity and solar weighted absorption fraction of nanofluids**

Run	Input Variables		Responses	
	ATO/Ag (% mass fraction)	SDS (% mass fraction)	Solar Weighted absorptivity (%) (Error range $\pm 1.01\%$)	Thermal conductivity ($\text{Wm}^{-1}\text{K}^{-1}$) (Error range $\pm 5\%$)
1	0.01	0.15	53.05	0.64
2	0.11	0.15	85.15	0.6654
3	0.11	0.1	91.63	0.65941
4	0.11	0.15	83	0.665
5	0.11	0.15	82.5	0.6656
6	0.04	0.11	74.03	0.64808
7	0.17	0.19	95.05	0.6665
8	0.11	0.2	82.6	0.65941
9	0.04	0.19	70.289	0.6491
10	0.17	0.11	93.54	0.667
11	0.2	0.15	98.9	0.67
12	0.11	0.15	84	0.6655
13	0.11	0.15	85.99	0.6654

263 The analysis is done in the wavelength corresponding to the solar spectrum ranging from visible
 264 to NIR range (280-1200 μm). The optical path length of the beam is fixed as 10 mm. Beer-Lamberts

265 law given by Eq. (1) is used to find the extinction coefficient (K_e) of nanofluid from spectral
 266 transmittance coefficient ($\tau(\lambda)$), assuming that reflection and scattering are negligible.

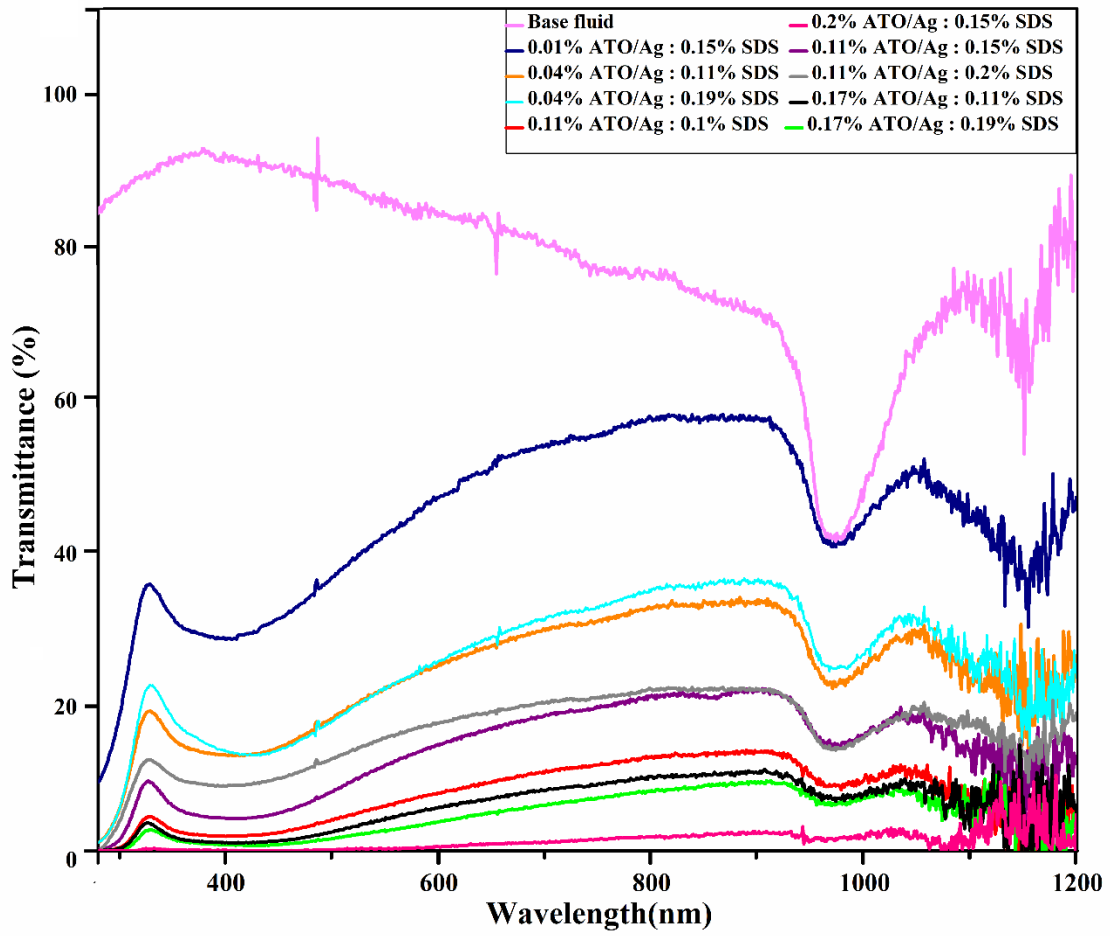
$$\tau_\lambda = e^{-yK_e} = 1 - \alpha_\lambda \quad (1)$$

267 Transmittance spectra of nanofluids and the base fluid are shown in Fig. 6. The transmittance of
 268 nanofluid is compared with base fluid to indicate the decrease in transmittance ratio along the
 269 spectrum. Transmittance exhibited by nanofluid samples is showing a steep decrease at visible
 270 spectrum (350 nm – 450 nm) and NIR spectrum (950 nm – 1050 nm). This decrease in
 271 transmittance is due to the synergetic effect of ATO/Ag hybrid nanofluid having absorption peaks
 272 in the visible region (400 nm) and NIR region (1000 nm). Transmittance spectra can be considered
 273 to verify the presence of materials with absorption peaks in these above reported spectral range.
 274 From the transmittance spectra, radiative transmittance is observed to be a descending function of
 275 nanoparticle mass fraction. The highest transmittance is produced by the nanofluid with the least
 276 concentration (0.01% ATO/Ag). Least transmittance was provided by nanofluid with maximum
 277 nanoparticle mass fraction (0.2% ATO/Ag). For two samples, Run 6 (0.04% ATO/Ag 0.19%
 278 SDS) and Run 9 (0.04% ATO/Ag 0.11% SDS), with the same mass fraction of ATO/Ag,
 279 transmittance was found to be lower for the sample with lesser surfactant mass fraction. This trend
 280 of higher absorption at lower surfactant concentration is repeating for the two other samples, Run
 281 7 (0.17% ATO/Ag, 0.19% SDS) and Run 10 (0.17% ATO/Ag, 0.11% SDS), with the same mass
 282 fraction. Noise observed in transmittance spectra above 1100 nm is due to the instrument.

283 The percentage of solar energy absorbed by the nanofluid volume is represented by
 284 the solar-weighted absorption fraction (S_m) calculated using Eq. (2) suggested by Drotning [32].

$$S_m = \frac{\int_0^\lambda I_\lambda \alpha_\lambda d\lambda}{\int_0^\lambda I_\lambda d\lambda} \quad (2)$$

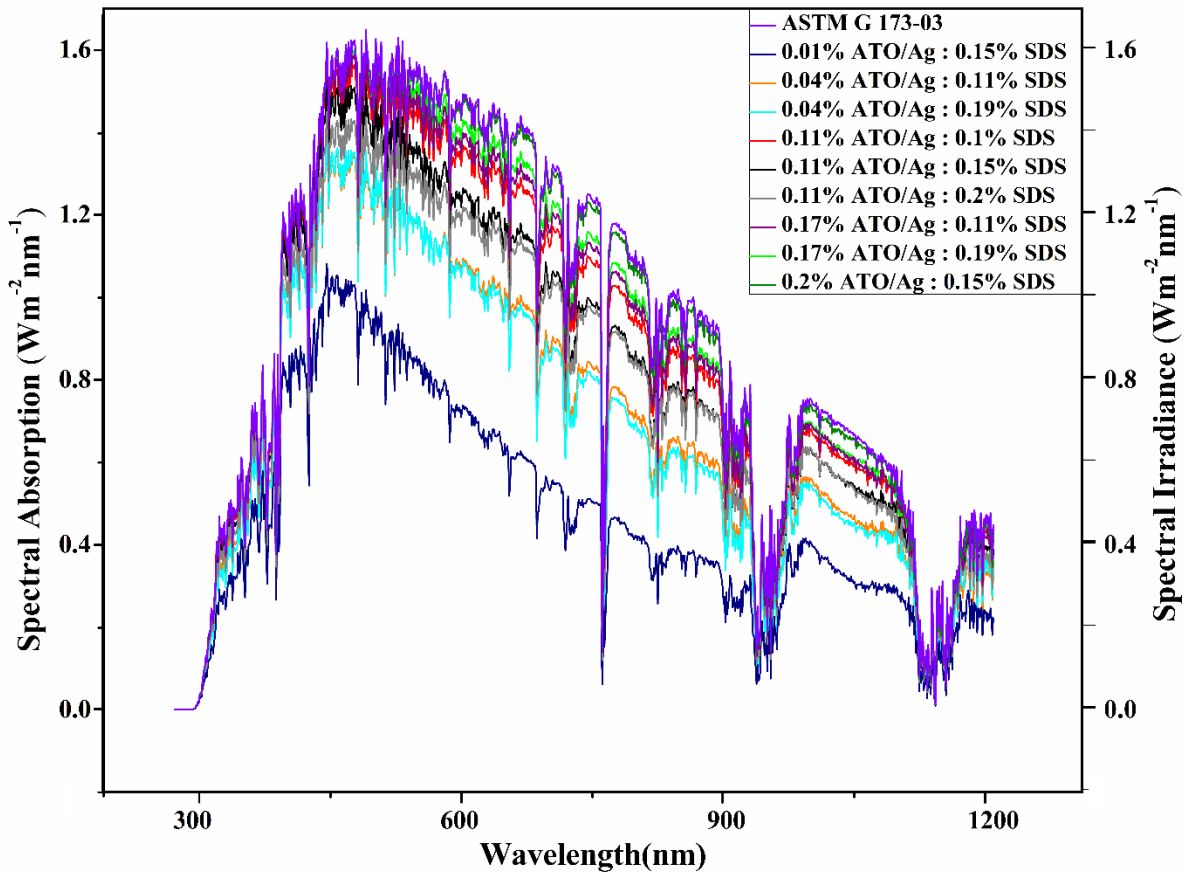
285 Fig. 7 depicts the spectral solar irradiance of nanofluid samples along with the reference spectrum.
 286 ASTM G-173 [32] at AM 1.5 standard is used as the reference spectra. Solar weighted absorptivity
 287 graph, when coinciding with reference spectra indicates a 100% radiation absorption by a
 288 nanofluid. The maximum solar absorption of 98.90% is displayed by Run 11 corresponding to the
 289 sample with the highest nanoparticle mass fraction (0.2%). The lowest spectral absorption is
 290 showed by the sample (Run 1) with the least concentration of nanoparticle (0.01%).



291

292

Fig. 6. Transmittance of nanofluid samples (Run 1, 2, 3, 6, 7, 8, 9, 10, 11) and water



293

294

Fig. 7. Spectral irradiance of reference and nanofluid samples

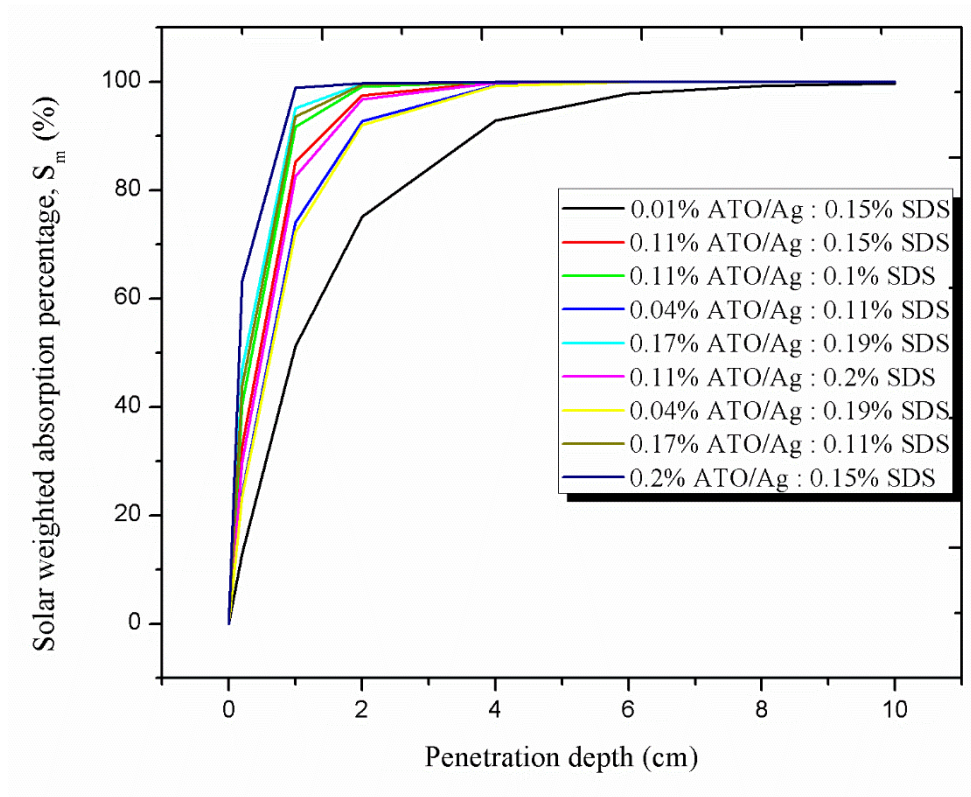
295 **4. Parametric study**

296 *4.1. Effect of penetration depth on solar weighted absorption fraction*

297 The transmittance of nanofluid decreases with an increase in the penetration depth of radiation.
 298 Beer-Lambert law was used for studying the dependence of solar weighted absorption fraction on
 299 penetration depth. As observed in Fig. 8, the solar weighted absorption fraction is increasing
 300 exponentially with an increase in penetration distance. The influence of penetration depth on solar
 301 weighted absorption fraction is studied in a range of 0.2 - 10cm. Longer penetration distance
 302 provides improvement in solar weighted absorption fraction even though the concentration of
 303 nanofluid is less. Run 1 is having the lowest value of S_m at each penetration depth. From the
 304 variation of S_m plotted it is clearly observed that nanofluid with lesser concentration of

305 nanoparticles at shorter penetration depth is not preferred. A higher concentration of nanoparticle
306 at longer penetration depth is also not advisable as the chances of agglomeration are prevalent.

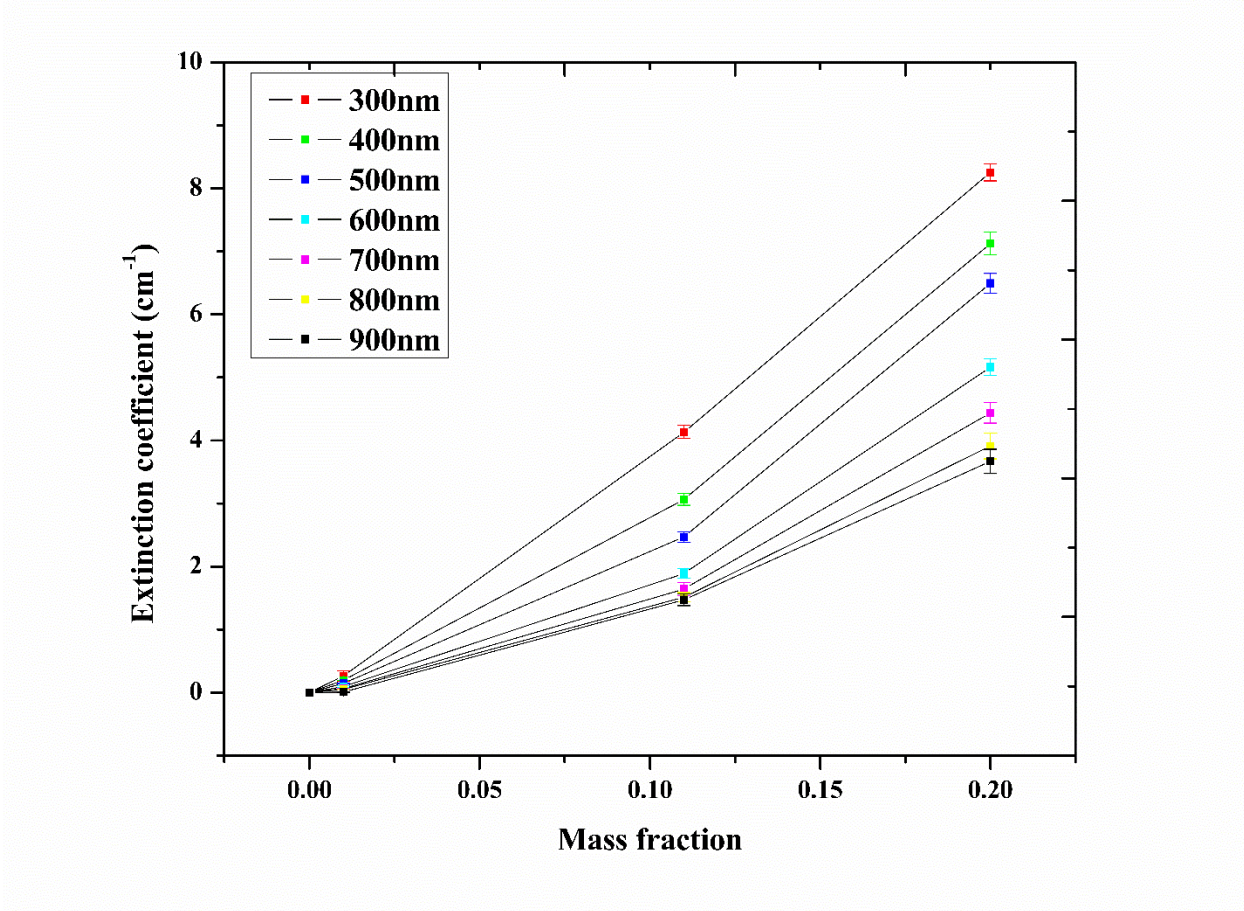
307 Nanofluids with nanoparticle concentrations of 0.11% and above are having a solar
308 weighted absorption percentage of 90 - 100% for penetration depth above 1.5 cm. Therefore, the
309 dimension for nanofluid receiver volume must be above the optimum depth of penetration. The
310 depth of penetration is not preferred to be increased much beyond the optimum depth as heat losses
311 increase with an increase in surface area. Also, at higher optical path length, the complete radiation
312 will be absorbed above a certain height and the resultant heat developed would have to be
313 conducted to the remaining volume. Hence, it can be concluded that the optimum concentration at
314 optimum penetration depth is required. In the present PTDASC system, since the inner diameter
315 of the glass tube is 1.5 cm, it can be ensured that the extinction taking place in the fluid volume is
316 greater than 95% for nanofluids with nanoparticle concentrations of 0.11% and above.



317
318 **Fig. 8.** Variation of solar weighted absorption percentage with penetration depth

319 4.2. *Effect of mass fraction on the extinction coefficient*

320 The effect of the mass fraction of nanoparticle on the extinction coefficient of nanofluid was
321 investigated and plotted as given in Fig. 9. The investigations were performed on concentrations
322 of nanoparticles corresponding to maximum (0.2%), average (0.11%) and minimum (0.01%), at
323 wavelengths ranging from 300 nm to 900 nm. As observed in Fig. 9, the extinction coefficient is
324 observed to be approximately a linear function of the mass fraction. Hence, absorption efficiency
325 is increasing with optical path length for a specified concentration and, with increasing
326 concentration for a specified light path length. Surmising from the parametric analysis, the solar
327 radiation can be absorbed by either increasing the concentration or optical depth of penetration.
328 By controlling the mass fraction of nanoparticle, the solar radiation can be absorbed completely
329 for a specific optical depth. An error bar is also provided with the extinction curve to show the
330 deviation involved in the measurement of values.



331

332 **Fig. 9.** Variation of extinction coefficient with mass fractions of nanoparticle

333 **5. Optimization of mass fraction using Response surface methodology**

334 *5.1. ANOVA analysis of Solar Weighted Absorption Fraction*

335 Analysis of variance (ANOVA) of the solar weighted absorption fraction is presented in Table 3,
 336 which provides information on the significant parameters in the designed model. The model is
 337 significant as the p-value is less than 0.0001. A, B, A² and AB² are the significant model terms as
 338 their p-value is less than 0.1. ATO/Ag nanoparticle concentration is the most significant
 339 independent parameter among the factors since it is having the highest F value. The lack of fit
 340 being insignificant indicates that the model obtained is a correct fit. The difference between
 341 predicted R-squared and adjusted R-squared being less than 0.2, as shown in Table 6, implies the
 342 terms are in agreement. Furthermore, the value of R-squared and adjusted R-squared which are
 343 0.9839 and 0.9678 respectively, implies the model is fitting perfectly. Adequate-precision, which
 344 measures the signal to noise ratio, is greater than the desired value of 4. The coefficient of
 345 determination (R-squared) value obtained was found to be greater than the good-fitting criterion
 346 of 0.8. Finally, the standard deviation of 2.16 points out the accuracy of the experiments.

347 **Table 3:** ANOVA of solar weighted absorption fraction

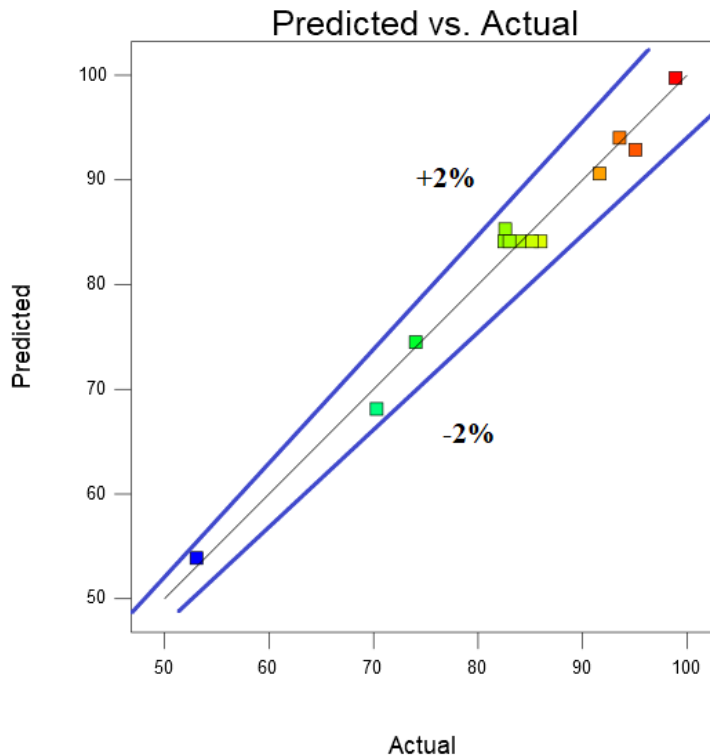
Source	Sum of Squares	Df	Mean Square	F Value	p-value Prob > F	Significance
Model	1709.55	6	284.93	61.07	< 0.0001	Significant
A-ATO/Ag	1051.11	1	1051.11	225.28	< 0.0001	
B-Surfactant	28.13	1	28.13	6.03	0.0494	
AB	6.89	1	6.89	1.48	0.2698	
A ²	92.98	1	92.98	19.93	0.0043	
B ²	25.49	1	25.49	5.46	0.0581	
AB ²	52.89	1	52.89	11.34	0.0151	
Residual	28.00	6	4.67			
Lack of Fit	19.54	2	9.77	4.63	0.0911	not significant
Pure Error	8.45	4	2.11			
Cor Total	1737.55	12				

Std. Dev.	2.16	R ²	0.9839
Mean	83.06	Adjusted R ²	0.9678
C.V. %	2.60	Predicted R ²	0.8161
PRESS	319.55	Adequate Precision	28.926

348 An empirical correlation for solar weighted absorption fraction which was obtained from the model
 349 developed for predicting responses for each level of factors, is given by Eq. (3). The significance
 350 of the various factors cannot be inferred from coefficients in the equation as they are scaled to the
 351 appropriate unit. As observed from Fig. 10, the values of solar weighted absorption fraction
 352 obtained from experimental data and model predicted values are in good agreement. The error was
 353 observed to be falling within $\pm 2\%$.

$$\begin{aligned} \text{Solar Weighted Absorption Fraction} = & + 245.66320 - 1049.46831 * ATO/Ag - \\ & 2499.66608 * Surfactant + 18926.22192 * ATO/Ag * Surfactant - \quad (3) \\ & 810.18006 * (ATO/Ag)^2 + 7961.96978 * (Surfactant)^2 - 61244.95027 * \\ & ATO/Ag * (Surfactant)^2 \end{aligned}$$

Design-Expert® Software
 Solar Weighted Absorption Fraction
 Color points by value of
 Solar Weighted Absorption Fraction:
 98.9
 53.05



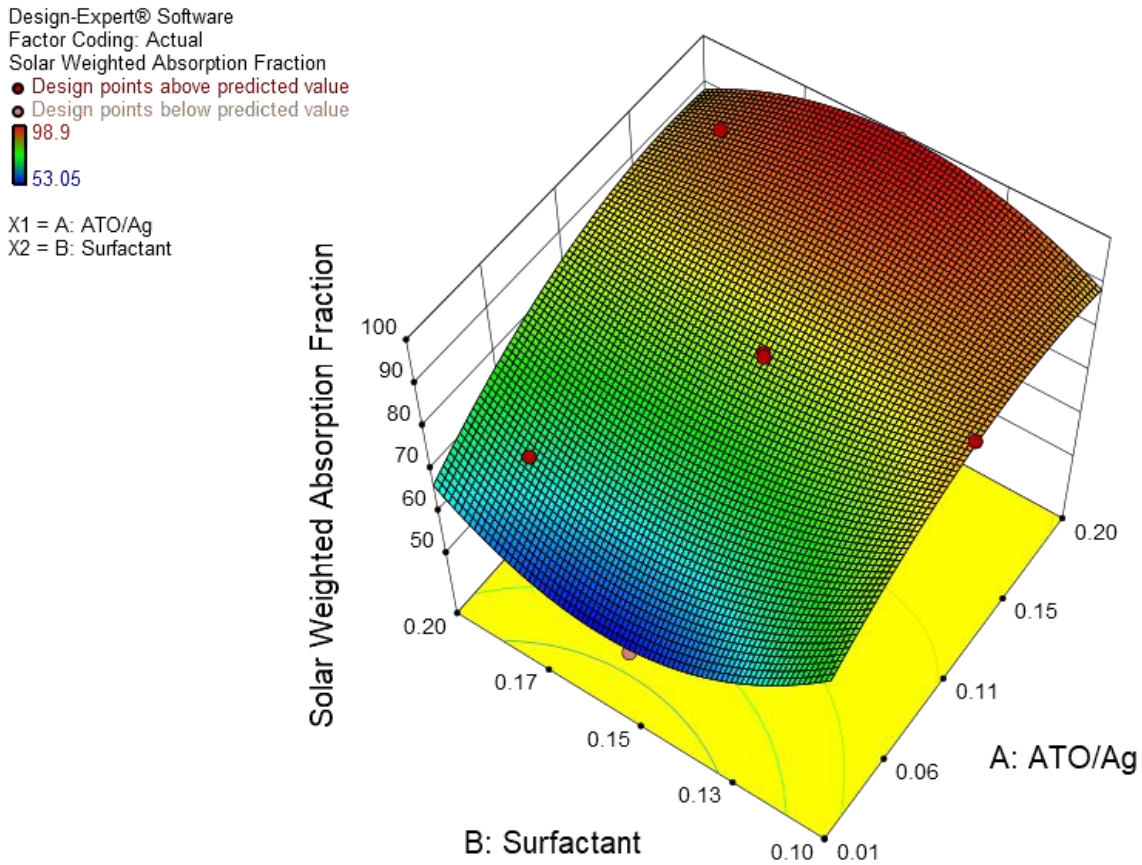
354
 355

Fig. 10. Comparison between predicted values and actual values of S_m

356 5.2. Interaction effect of process parameters on Solar weighted absorption fraction

357 The 3D plot of absorption fraction with respect to ATO/Ag and SDS mass fraction, given by Fig.
358 11, clearly specifies that even though absorptivity increases with an increase in nanoparticle
359 concentration, the extreme surfactant concentration is seen to influence the absorption fraction. At
360 minimum nanoparticle concentration, the absorption fraction is observed to be higher at the highest
361 and the lowest surfactant concentration. The absorption fraction tends to increase with ATO/Ag
362 nanoparticle concentration and then decreases at maximum nanoparticle concentration, for both
363 high and low surfactant concentrations.

364

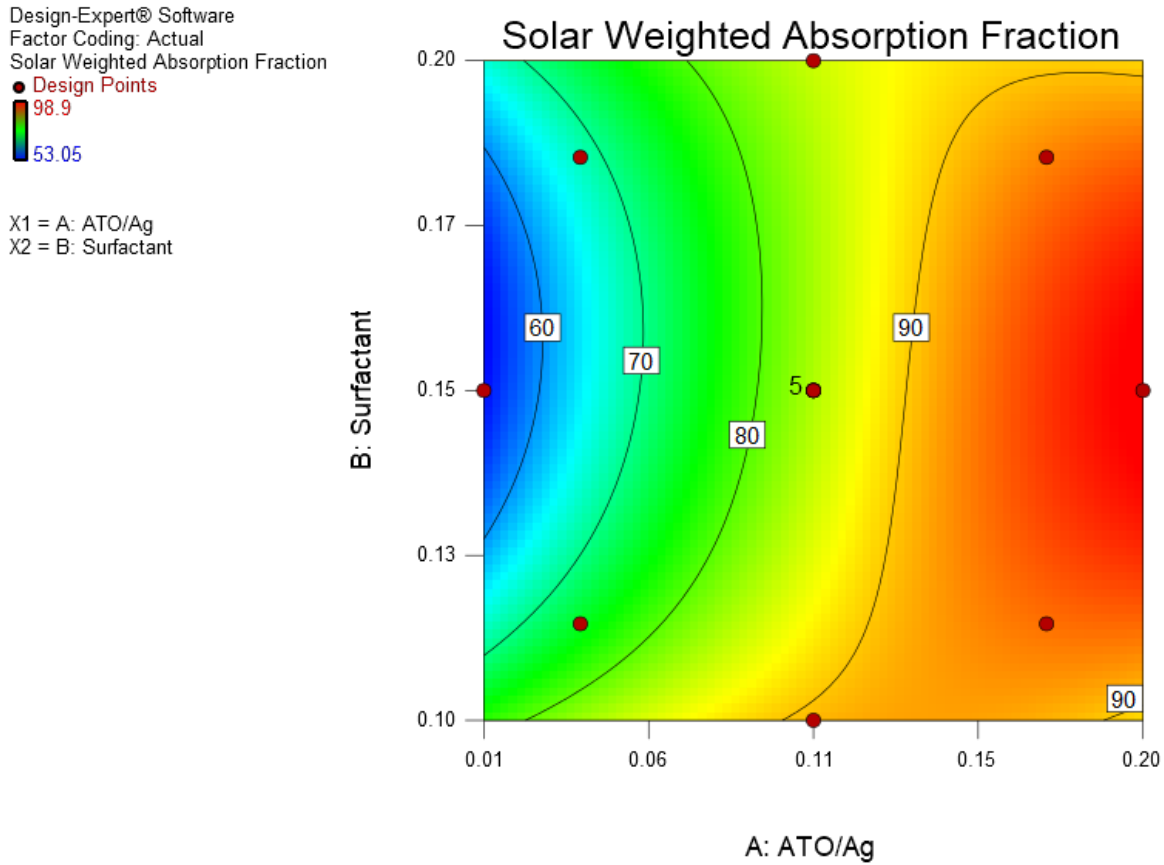


365

366 **Fig. 11.** Interaction effect of ATO/Ag and surfactant mass fractions on S_m : 3D surface.

367 As seen from the 2D plot of factors given by Fig. 12, ATO/Ag mass fraction is having the most
368 influence on solar weighted absorption fraction. The maximum absorption fraction of 98.9%

369 occurs at the highest concentration of nanofluid. For the samples Run 7 (0.17% ATO/Ag - 0.19%
 370 SDS) and Run 10 (0.17% ATO/Ag - 0.11% SDS), having the same nanoparticle mass fractions,
 371 the solar weighted absorption fraction was calculated to be 95% and 93.5% respectively. Hence
 372 the effect of surfactant concentration on solar weighted absorption is minimal.



373

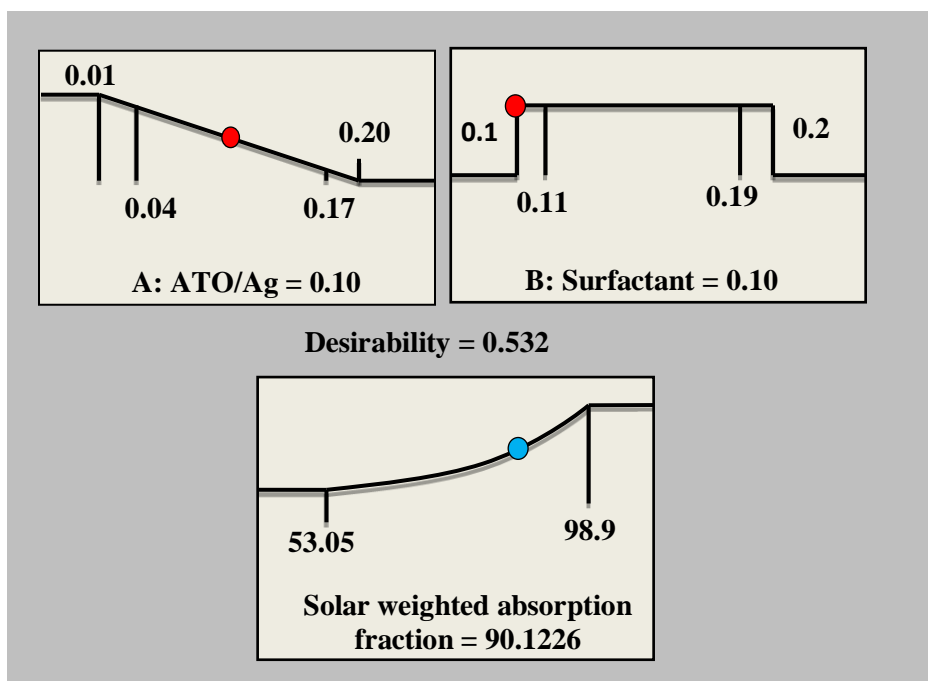
374 **Fig. 12.** Interaction effect of ATO/Ag and surfactant mass fractions on S_m : contour plot.

375 As discussed in Section 3.2, since the enhancement in thermal conductivity by the addition of
 376 nanoparticles was falling in the uncertainty range of the instrument, the optimization was
 377 performed based on a single response variable i.e. solar weighted absorption fraction.

378 *5.3. Optimization of variables using desirability function*

379 The DOE model was created for statistically optimizing the response variables to obtain an
 380 optimum value of inputs. From the model developed, solar weighted absorption fraction at each

381 factor levels are also obtained. Desirability is the objective function used for optimization. The
 382 weightage for variables can be adjusted on a scale of 1 to 5 [27, 34 and 35]. Increasing the
 383 weightage drives the output response towards the desired goal. Weightage of 3 was provided for
 384 solar weighted absorption fraction [35]. Desirability ranges from a minimum of zero to a maximum
 385 one. The maximum desirability provided by an operating condition is found by numerical
 386 optimization and was obtained as 0.532. The optimized concentrations of both ATO/Ag and SDS
 387 were obtained as 0.10%. The solar weighted absorption fraction predicted for the optimized
 388 condition is 90.12%. The weighted absorption fraction for the obtained optimum mass fraction
 389 was calculated experimentally and found to be 89% which is having a negligible error of 1.2%
 390 with the predicted value.



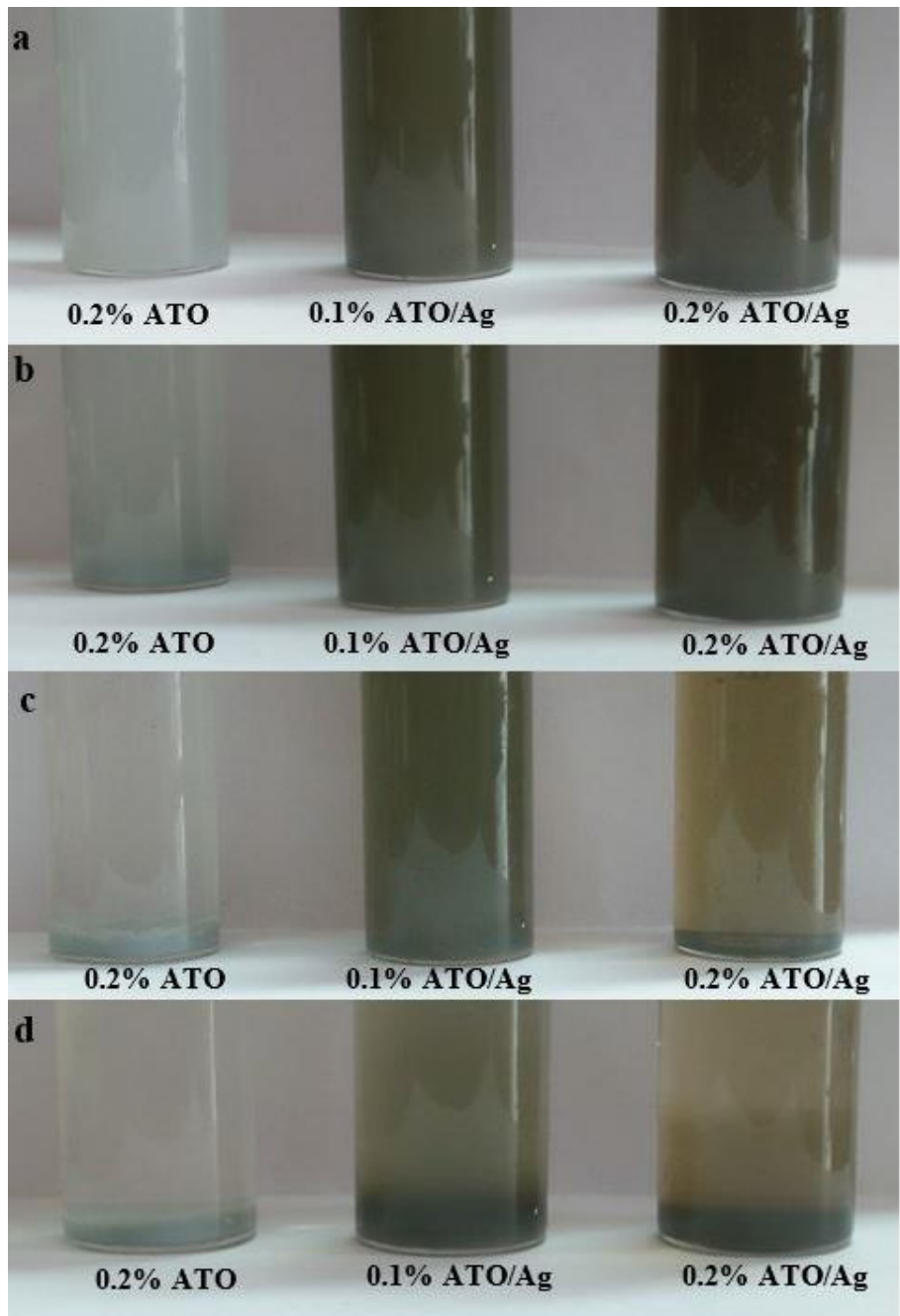
391

392 **Fig. 13.** Ramp function graph of desirability for numerical optimization

393 *5.4. Stability analysis of optimized nanofluid*

394 The sedimentation method was employed for investigating the stability of nanofluid [36] as shown
 395 in Fig. 14. On visual inspection, the ATO/Ag hybrid nanofluid was found to possess better stability
 396 compared to ATO nanofluid. The settling of ATO nanoparticles was prominent after 7 days from
 397 the synthesis date. Complete segregation of ATO nanoparticles was observed within 30 days after
 398 the synthesis. The optimized nanofluid (0.1% ATO/Ag) and nanofluid sample with maximum

399 concentration (0.2% ATO/Ag) exhibited better stability for 30 days with negligible segregation.
400 The optimized concentration was found to have achieved better dispersion stability compared to
401 nanofluid with 0.2% mass fraction for a longer time duration of 150 days.



402
403 **Fig. 14.** Visual inspection on the stability of nanofluid after synthesis for a period of (a) 30
404 minutes (b) 7 days (c) 30 days (d) 150 days

405 **6. Experimentation on Parabolic trough direct absorption solar collector**

406 *6.1. Reflector and absorber tube*

407 The solar thermal collector system consists of a parabolic shaped reflector mirror, a glass cover
 408 and a receiver tube placed at the focal point of the reflector. The focal point is at a distance of 0.27
 409 m from the vertex. The parabola and receiver dimensions are given in Table 5. The receiver tube
 410 is a quartz tube with high optical transmittance. A glass cover was used for preventing the
 411 convective heat loss from the receiver tube surface to the environment. The annular space is filled
 412 with air and sealed at both ends to prevent the effect of wind. The working fluid is flowing inside
 413 the receiver tube. Volumetric absorption of the concentrated solar rays occurs inside the fluid
 414 volume in the receiver tube. The shape and focal point of parabolic reflectors are given by Eq. (4)
 415 and Eq. (5) respectively.

$$y = 0.925x^2 \tag{4}$$

$$f = \frac{W_a}{2} \cot \varphi_r + \frac{W_a^2}{16f} \tag{5}$$

F Focal distance (m)

W Aperture width (m)

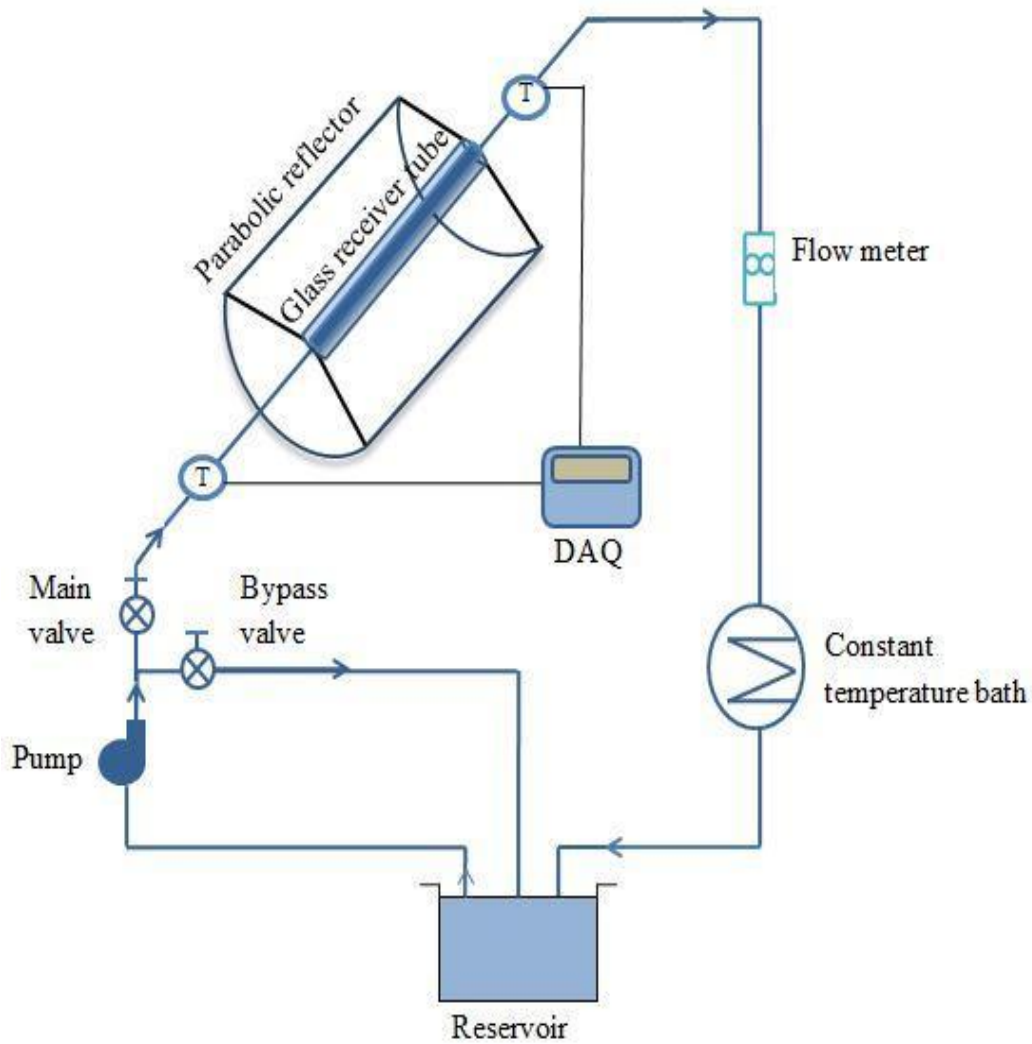
φ Rim angle (degree)

416 **Table 5: Dimensions of the receiver tube**

Parameters	Dimensions
Absorber tube inner diameter	15 mm
Absorber tube outer diameter	18 mm
Glass cover inner diameter	36 mm
Glass cover outer diameter	40 mm
Length of the receiver tube	1500 mm
Aperture width	1080 mm
Focal point	270 mm

417 6.2. Hydraulic cycle

418 The hydraulic cycle of the collector system was based on ASHRAE Standard 93-2010 as shown
419 in Fig. 15. The fluid flow is controlled using the main valve and a bypass valve. The bypass valve
420 was installed for the low flow rates according to the ASHRAE standards. The concentrated solar
421 radiation is absorbed by the nanofluid while passing through the receiver tube. The temperatures
422 at the inlet and exit were measured using calibrated T-type thermocouples with an accuracy of 0.5
423 °C. Rotameter present at the flow outlet will measure the fluid flow rate through the cycle. The
424 absorbing fluid enters the heat exchanger to reject heat and is pumped back through the cycle.
425



426
427

Fig. 15. The schematic of the hydraulic cycle

428 The actual experimental setup is shown in Fig. 16. A single-axis solar tracking was performed for
429 the experiment. The automated solar tracker aligns the position of the reflector directly towards
430 the radiation. The incidence angle is having a predominant effect on the thermal efficiency of the
431 collector [37]. Hence, after experimenting on a range of incidence angles between 0° and 20° , the
432 inclination equal to the incidence angle (11.3°) was found to be providing higher efficiency.
433 Providing an inclination equal to the incidence angle, will decrease the shadowing at the ends and
434 allows direct solar irradiation. The solar intensity was measured using an industrial standard
435 pyranometer with an accuracy of $\pm 5W^{-2}$.

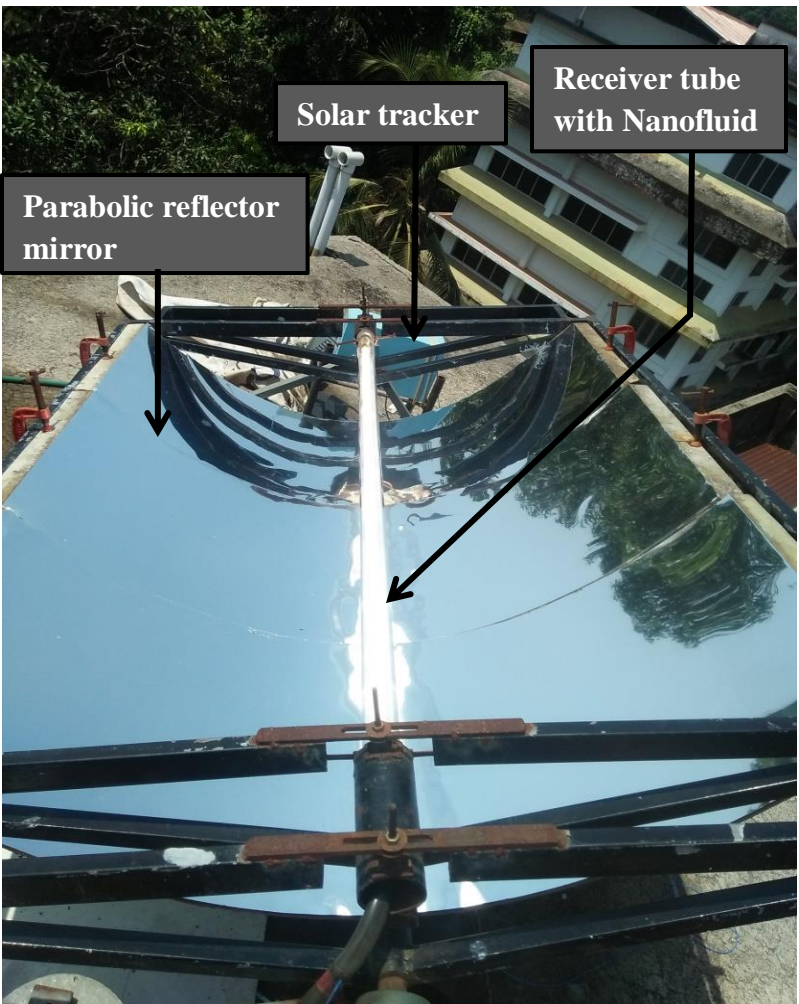


Fig. 16. Experimental setup of PTDASC

436
437
438
439
440

441 6.3. Performance evaluation methodology of PTDASC

442 6.3.1. Thermal efficiency

443 Instantaneous thermal efficiency was calculated at a time step of 5 minutes during the test day.
 444 Thermal efficiency calculated using Eq. (6), is the ratio between useful thermal energy of nanofluid
 445 to the total energy received by the parabolic trough collector.

$$\eta_{th} = \frac{\dot{m}C_{p,h}\Delta T}{IA} \quad (6)$$

446 6.3.2. Optical efficiency

447 The optical efficiency of the collector is obtained by considering all the optical materials that are
 448 occurring in the path of the light beam. Geometric and intercept factors need to be found out for
 449 calculating the optical efficiency using Eq. (7) [38]. Geometric factor, K, given by Eq. (8), is a
 450 measure of the effective reduction of the aperture area due to abnormal incidence effects. The
 451 intercept factor, γ , is the ratio of the energy intercepted by the receiver to the energy reflected by
 452 the reflector. A MATLAB code was generated to solve Eq. (9) using Simpson's one-third rule, to
 453 find the intercept factor. Geometric factor, intercept factors, and solar collector material properties
 454 were used to find the optical efficiency at each incidence angle using Eq. (7). The Intercept factor
 455 [39] was found to be 0.9228 from Eq. (9).

$$\eta_{optical} = (\rho_{collector}\tau_{cover}\alpha_{receiver}) * \gamma * (1 - A_f \tan \theta) \cos \theta \quad (7)$$

$$K = 1 - \left(\frac{D_{out}}{L_a} + \frac{f}{L_a} \left(1 + \frac{W_a^2}{48L_a^2} \right) \right) \tan \theta \quad (8)$$

$$\gamma = \frac{1+\cos\varphi_r}{2\sin\varphi_r} \int_0^{\theta_r} \operatorname{erf} \left(\frac{\sin\varphi_r(1+\cos\theta)(1-2a\sin\theta) - (\pi\beta(1+\cos\varphi_r))}{\sqrt{2}\pi\sigma(1+\cos\varphi_r)} \right) + \quad (9)$$

$$- \operatorname{erf} \left(-\frac{\sin\varphi_r(1+\cos\theta)(1+2a\sin\theta) + (\pi\beta(1+\cos\varphi_r))}{\sqrt{2}\pi\sigma(1+\cos\varphi_r)} \right) \frac{d\theta}{1+\cos\theta}$$

456 6.3.3. Exergy efficiency

457 Exergy is defined as the maximum useful work that can be extracted from a system at a given state
458 in a specific environment. Exergy analysis is crucial in analyzing the potential of solar thermal
459 systems.

460 Assumptions for exergy analysis:

- 461 1. Kinetic and potential energies are neglected
- 462 2. Chemical and nuclear interactions are neglected
- 463 3. Energy flow into the system and the work done by the system is taken as positive.
- 464 4. Exergy due to pressure drop is neglected.

465 Based on the assumptions stated above, an exergy balance across the receiver was formulated as
466 shown in the Eq. (10-15). The exergy efficiency of the PTDASC is given by Eq. (15). Exergy from
467 solar radiation and fluid flow are the significant contributing factors in the exergy balance of the
468 concerned PTDASC.

$$\Sigma\psi_{in} - \Sigma\psi_{out} = \psi_{dest} \quad (10)$$

$$\psi_{sol} + \psi_{m,in} - \psi_{m,out} = \psi_{dest} \quad (11)$$

469 Where the $\psi_{m,in}$ and $\psi_{m,out}$ are calculated by using Eq. 12 and Eq. 13 respectively.

$$\psi_{m,in} = (h_{in} - h_{amb}) - T_{amb}(s_{in} - S_{amb}) \quad (12)$$

$$\psi_{m,out} = (h_{out} - h_{amb}) - T_{amb}(s_{out} - S_{amb}) \quad (13)$$

470 Incident solar power received by the parabolic collector is obtained by multiplying the collector
471 aperture area with instantaneous solar radiation intensity as given by Eq. (14).

$$Q_{sol} = IA \quad (14)$$

472 Parabolic trough utilizes only beam radiation which can be assumed to be undiluted. Petela's
 473 exergy efficiency model [40] was used for finding the maximum power available from the incident
 474 solar radiation. The Sun was taken as the radiation reservoir which is having a temperature of
 475 5770K. The maximum work potential from solar radiation is calculated by multiplying the solar
 476 exergy efficiency with incident solar power, as shown in Eq. (15).

$$\psi_{sol} = \left(1 - \frac{4T_{amb}}{3T_s} + \frac{1}{3} \left(\frac{T_{amb}}{T_s}\right)^4\right) * IA \quad (15)$$

477 The Eq. (16), as described below, is obtained by substituting Eqs. (12), (13) and (15) in Eq. (11).

$$\psi_{dest} = \psi_{sol} - \dot{m}C_p \left((T_{out} - T_{in}) - T_{amb} \ln \left(\frac{T_{out}}{T_{in}} \right) \right) + \frac{\dot{m}T_{amb}\Delta P}{\rho T_{fm}} \quad (16)$$

478 The irreversibility term due to pressure drop in Eq. (16) can be ignored as the effect is less
 479 significant [41]. The higher density of liquid working fluids, compared to gaseous ones, account
 480 for the fact that irreversibility due to pressure drop in parabolic trough collector can be neglected
 481 while using liquid working fluids [42]. The exergy efficiency of the system is calculated using
 482 Eqn. (17).

$$\eta_{ex} = 1 - \left(\frac{\psi_{dest}}{\psi_{sol}} \right) \quad (17)$$

483 6.3.4. Uncertainty analysis

484 The uncertainty analysis was performed for quantifying the accuracy of the measurements. Error
 485 analysis was conducted to find the errors associated with the thermal efficiency and exergy
 486 efficiency. Uncertainties for thermal efficiency and exergy efficiency were calculated using the
 487 Moffat method [43] as described in Eq. 18 and Eq. 19 respectively. The uncertainty associated
 488 with measurement of temperature, incident solar radiation, and the flow rate is $\pm 1.4\%$, $\pm 0.625\%$
 489 and $\pm 2.5\%$, respectively. **The precision error occurring during the measurement of the extinction**
 490 **coefficient was taken into consideration and overall uncertainty in the measurement of the**
 491 **extinction coefficient was calculated to be $\pm 0.8\%$.** The mean uncertainty involved in the

492 calculation of the dependent parameters, thermal and exergy efficiency, was found to be $\pm 2.2\%$
 493 and $\pm 1.5\%$ respectively.

$$\frac{\delta\eta_{th}}{\eta_{th}} = \sqrt{\left(\frac{\delta m}{m}\right)^2 + \left(\frac{\delta\Delta T_{in}}{\Delta T_{in}}\right)^2 + \left(\frac{\delta\Delta T_{out}}{\Delta T_{out}}\right)^2 + \left(\frac{\delta I}{I}\right)^2} \quad (18)$$

$$\frac{\delta\eta_{ex}}{\eta_{ex}} = \sqrt{\left(\frac{\delta m}{m}\right)^2 + \left(\frac{\delta\Delta T_{in}}{\Delta T_{in}}\right)^2 + \left(\frac{\delta\Delta T_{out}}{\Delta T_{out}}\right)^2 + \left(\frac{\delta T_{amb}}{T_{amb}}\right)^2 + \left(\frac{\delta I}{I}\right)^2} \quad (19)$$

494 **6.4. Energy and Exergy analysis**

495 From Fig. 17, it is observed that the maximum optical efficiency of 75% is obtained when
 496 direct solar radiation is received at zero incidence angles. The various results of experimentation
 497 performed on nanofluid applied PTDASC at different flow rates are shown in Figs. 18, 19 and 20.
 498 The Figs. 18, 19 and 20 (c) illustrates the solar irradiation data received on each test day. The
 499 scattering observed in the energy and exergy efficiency curves in Figs. 18 and 19 (b) can be
 500 attributed to the thermal inertia during volumetric absorption. The variation in the solar irradiation
 501 received by the parabolic trough collector will affect the outlet temperature of the nanofluid which
 502 in turn produces the fluctuation in efficiency curves [44, 45]. The efficiency curve at the highest
 503 flow rate, Fig. 18 (b), shows that almost 90% of the data points corresponding to the instantaneous
 504 thermal efficiency of the solar collector was falling within a range of 40% to 60%. In the case of
 505 lower flow rates, the thermal efficiencies were varying in a smaller range which showed consistent
 506 results. The variation of instantaneous thermal and exergy efficiency with time for base fluid with
 507 flow rates of 0.016, 0.019 and 0.022 kgs⁻¹ is shown in Fig. 21 (a), (b) and (c) respectively. The
 508 variation in thermal and exergy efficiency of the hybrid nanofluid applied DASC with temperature
 509 difference across the receiver length was plotted for three different mass flow rates. The graphs
 510 Figs. 18, 19 and 20 (b), throws light on the dependence of efficiencies on the temperature
 511 difference attained. As observed in Fig. 18 (b), the thermal efficiency was increasing linearly with
 512 the rise in temperature difference across the tube length. Even though the exergy efficiency
 513 exhibited almost a similar trend as that of thermal efficiency, the highest exergy and thermal
 514 efficiencies were not occurring for the same nanofluid temperature gain. The highest exergy
 515 efficiency corresponded to the achievement of 8°C difference in nanofluid temperature across the
 516 system, while the peak thermal efficiency was pertaining to a rise of 12.6 °C. Also, in the case of

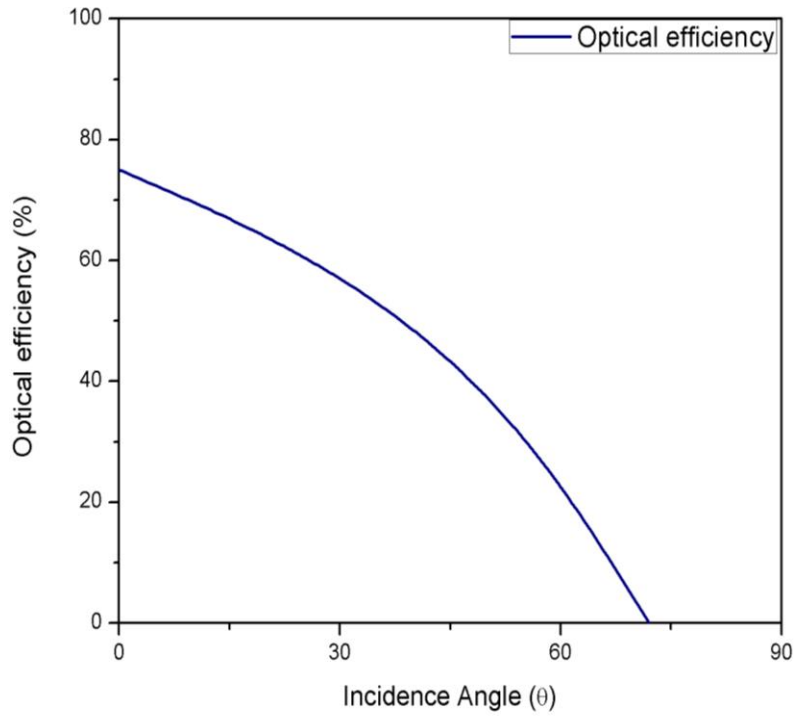
517 Fig. 19 and 20 (b), the trendlines of the efficiencies were almost parallel. The temperature
518 difference between the inlet and outlet of the receiver was observed to increase with a decrease in
519 the flow rate of the working fluids. The outlet temperature of the nanofluid increased by 3°C when
520 the flow rate was decreased from 0.022 kgs^{-1} to 0.016 kgs^{-1} .

521 From the experimental data obtained, the variation of thermal and exergy efficiency with solar
522 irradiation is plotted as shown in Fig. 22. Thermal and exergy efficiency was observed to increase
523 with the increase in solar irradiance. A decrease in the exergy efficiency was noticed with an
524 increase in solar irradiance above 800 Wm^{-2} while thermal efficiency was observed to increase. It
525 could be concluded that higher solar flux can produce more heat loss from the system. The effect
526 of heat loss on the exergy efficiency is higher compared to that of energy efficiency. Incident solar
527 irradiation was found to be having a predominant effect on the thermal efficiency enhancement
528 when compared with exergy efficiency. The variation of thermal and exergy efficiency of the
529 collector with flow rates is shown in Fig. 23. It is observed that the maximum efficiency of the
530 collector was pertaining to the maximum flow rate. The highest thermal efficiency and exergy
531 efficiency observed was 63.5% and 5.6% respectively at a flow rate of 0.022 kgs^{-1} . As the flow
532 rate increased from 0.016 kgs^{-1} to 0.019 kgs^{-1} and 0.022 kgs^{-1} , the thermal efficiency increased by
533 3.1% and 5.3% respectively, and the corresponding increase in exergy efficiency was 11.8% and
534 17.68%, respectively. The substantial rise in the exergy efficiency when compared to thermal
535 efficiency shows that the former is more dependent on solar irradiation while the latter is easily
536 controlled by flow rate. Hence optimization of the working parameters is required for the
537 collector's efficient performance. Exergy efficiency is dependent on the fluid inlet and outlet
538 temperatures, incident solar radiation and the ambient temperature. As the flow rate increases the
539 loss of heat from the collector is reduced as the time spent by nanofluid in the receiver is less.
540 Hence an increase in thermal and exergy efficiency will be observed. Also, the maximum nanofluid
541 outlet temperature increased with a decrease in flow rate. As the flow rate decreased, more energy
542 conversion took place due to absorption and scattering.

543 If the ambient temperature of the surrounding is high, then the exergy efficiency will be high
544 compared to the same conditions at lower ambient conditions. So, as the exergy varies due to more
545 factors compared to thermal efficiency, a linear relationship between these efficiencies could not

546 be stated from the results obtained. Also, the exergy efficiency is only important at inferring the
547 necessary heat loss reducing methods and not a factor at evaluating the applicability of the system.

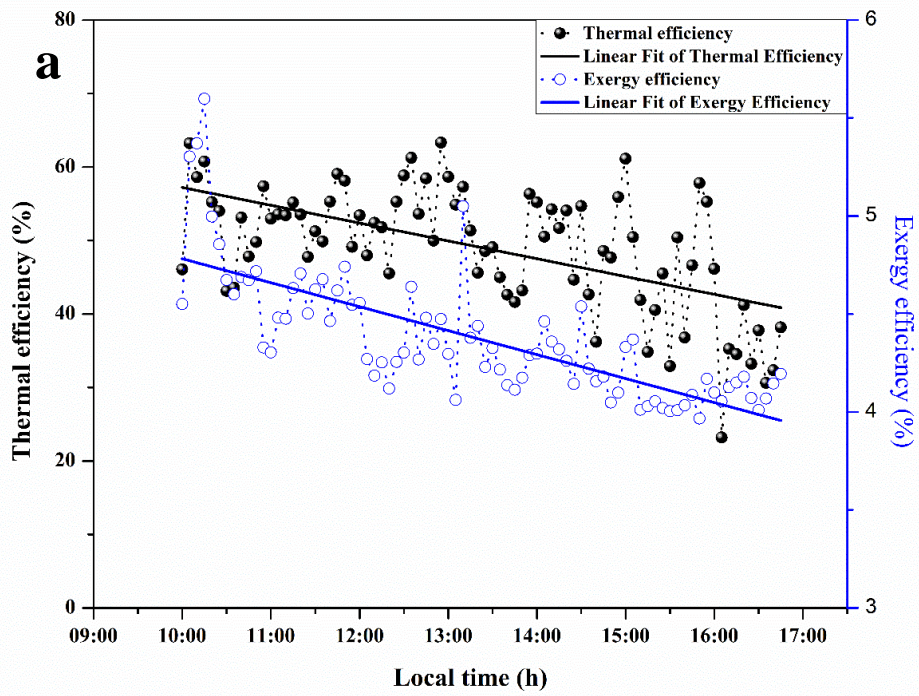
548



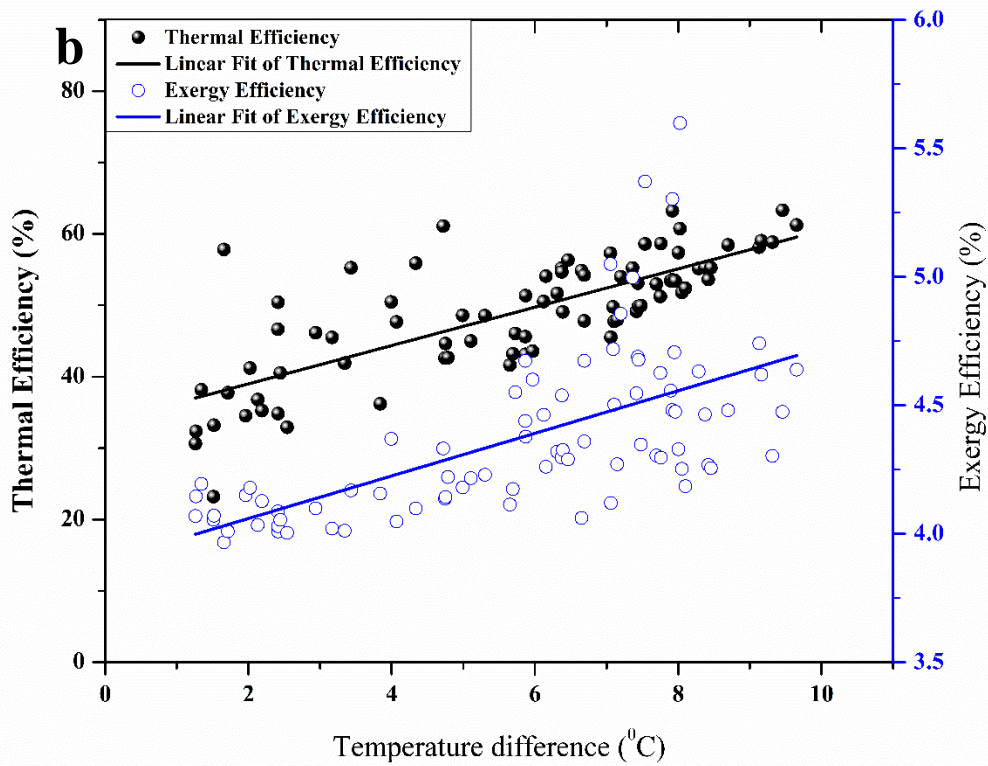
549

550

Fig. 17. Variation of optical efficiency with incidence angle

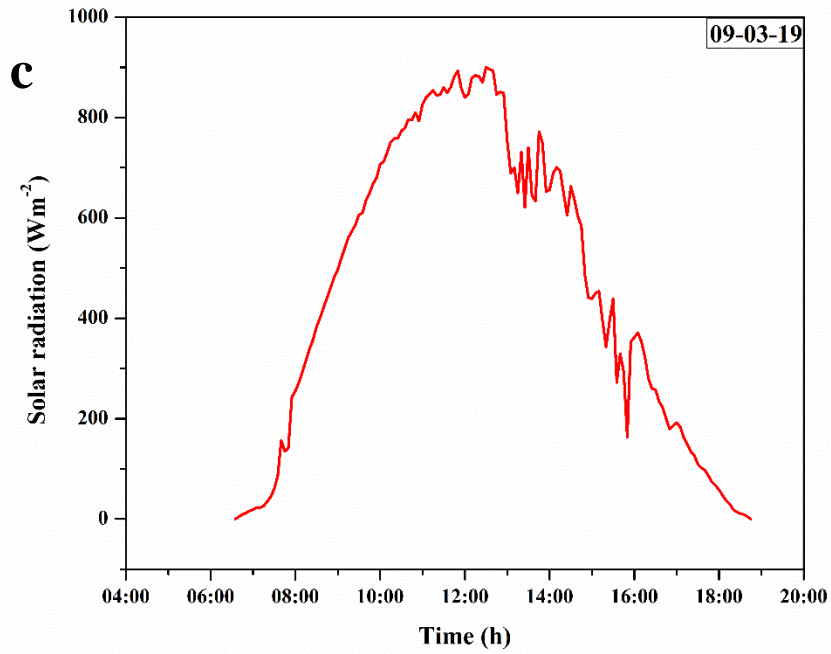


551



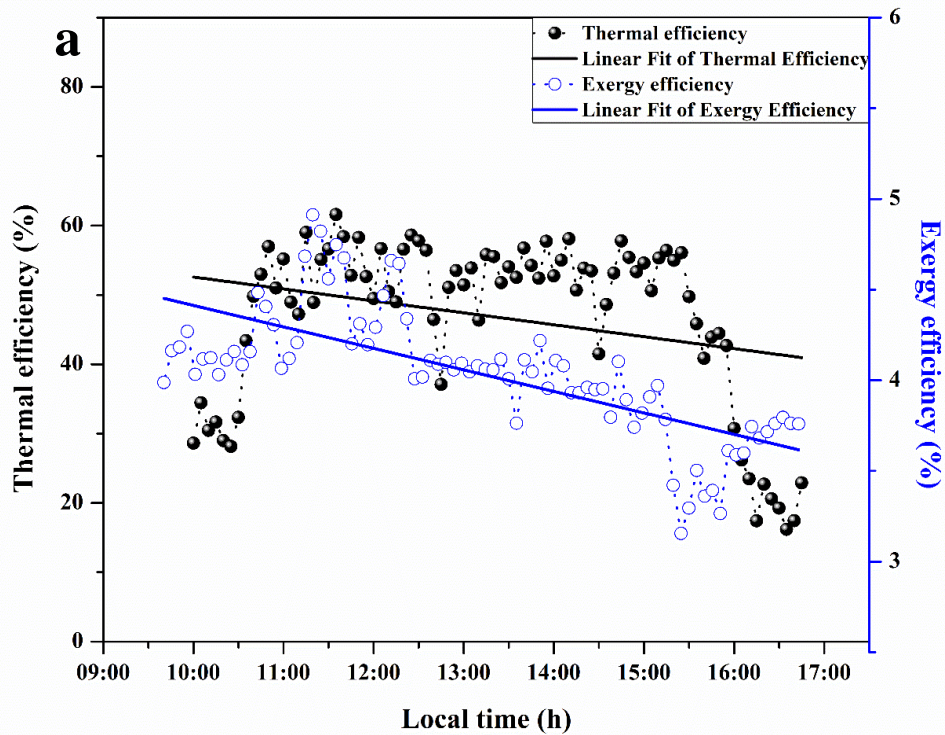
552

553

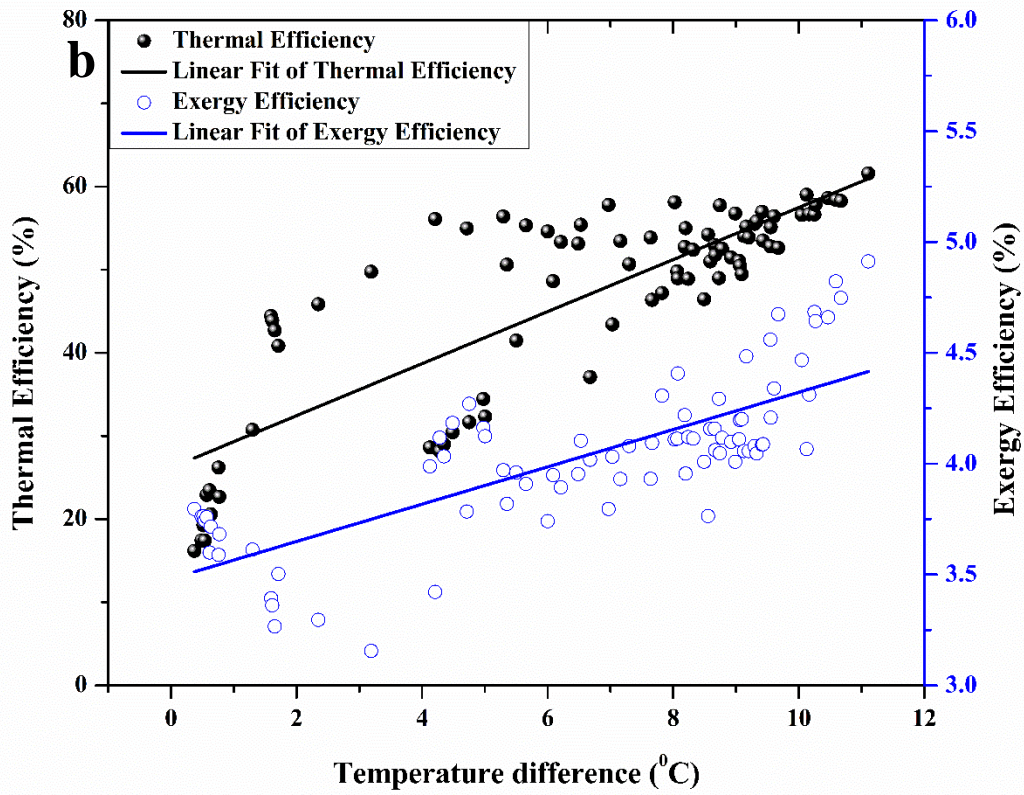


554

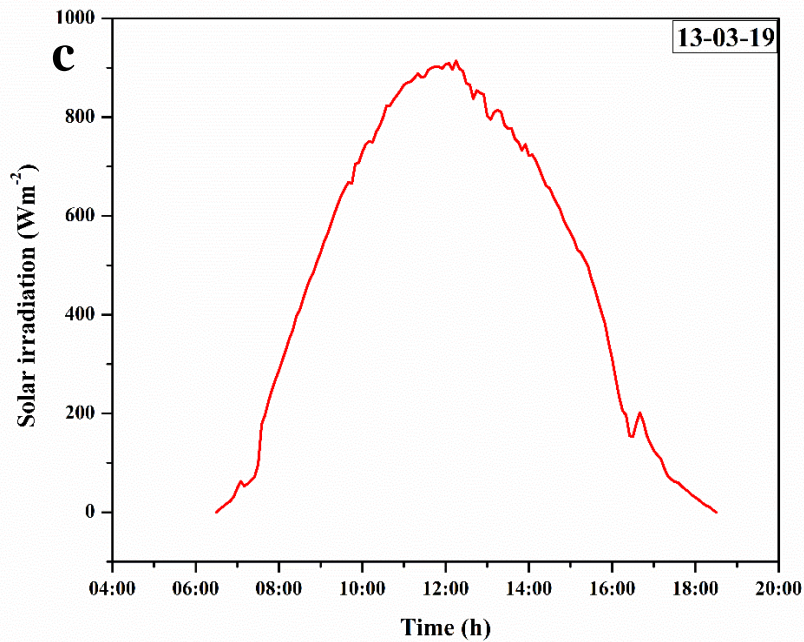
555 **Fig. 18.** (a) Thermal and exergy efficiency of PTDASC at 0.022 kgs^{-1} , (b) Variation of thermal
 556 and exergy efficiency with temperature difference (c) Solar radiation data for 09-03-19



557

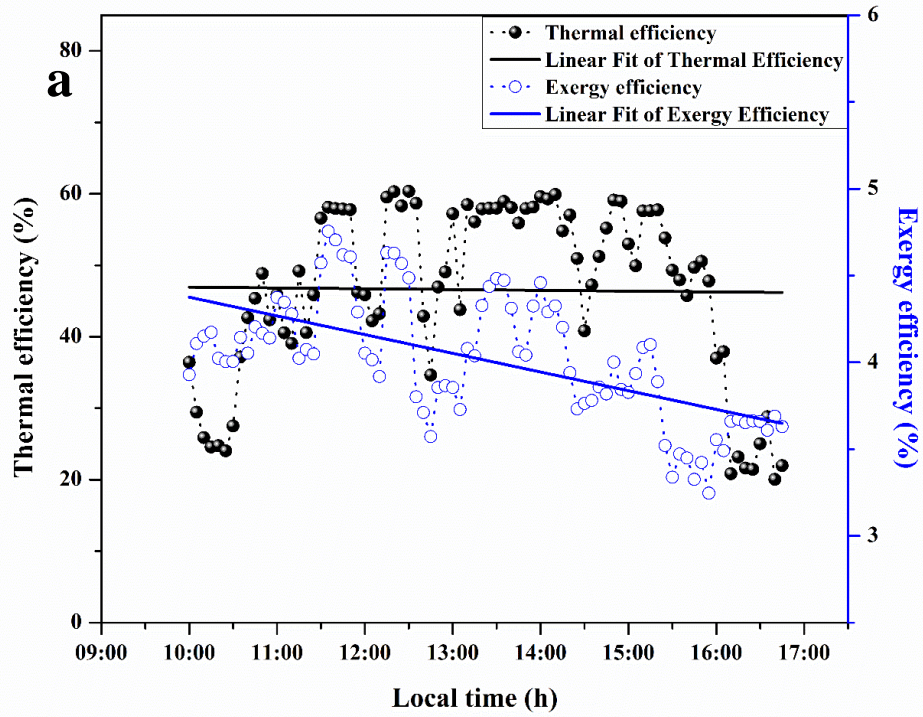


558

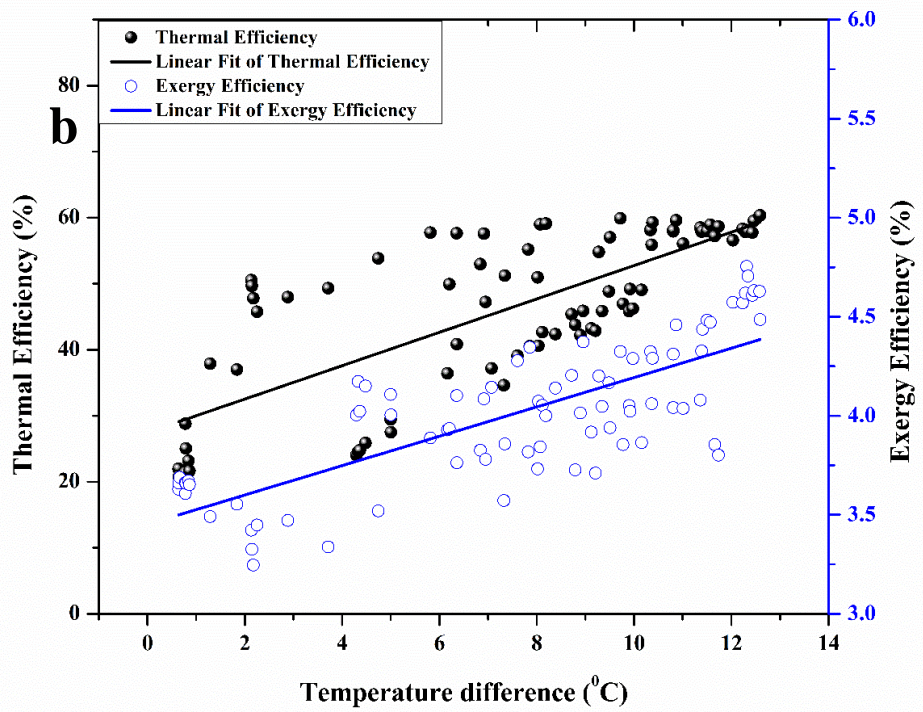


559

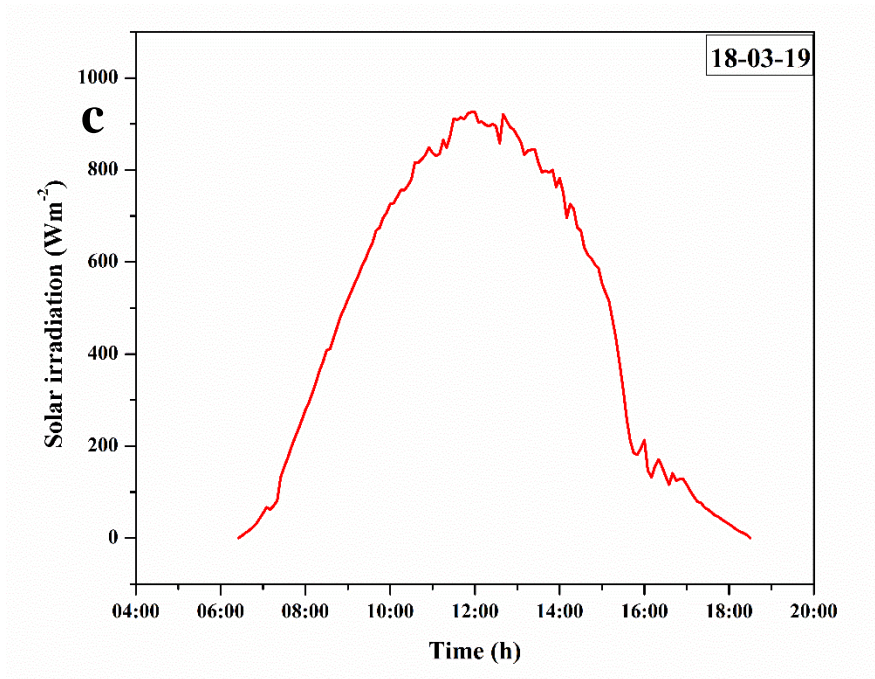
560 **Fig. 19.** (a) Thermal and exergy efficiency of PTDASC at 0.019 kgs^{-1} , (b) Variation of thermal
 561 and exergy efficiency with temperature difference (c) Solar radiation data for 13-03-19



562

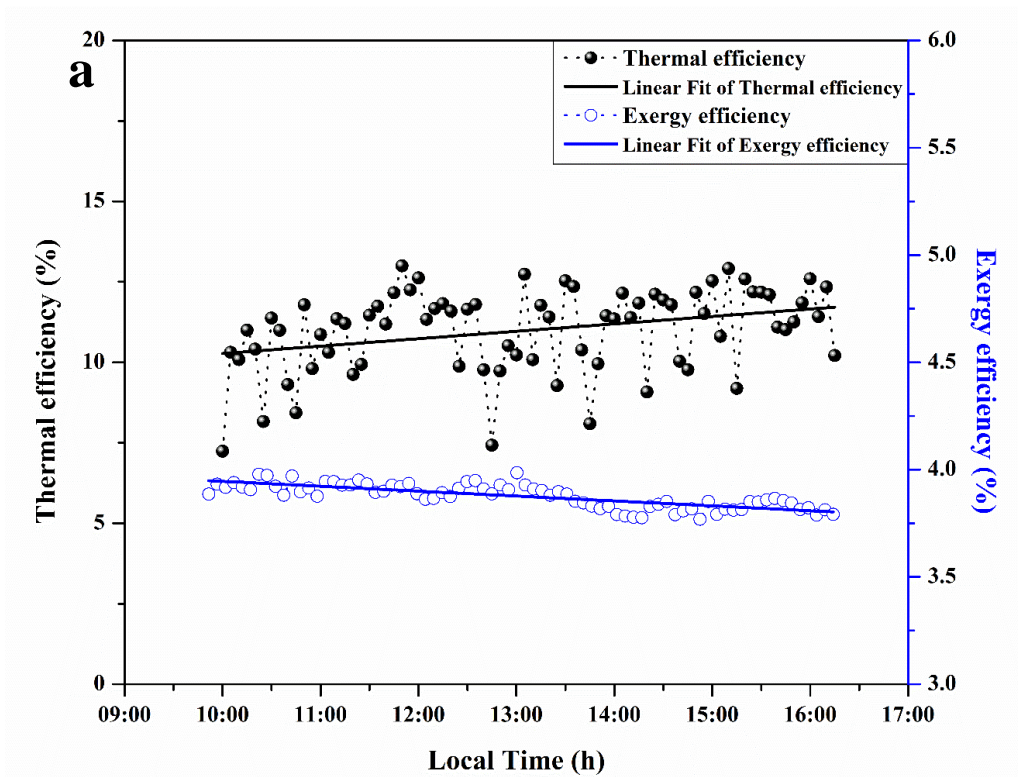


563

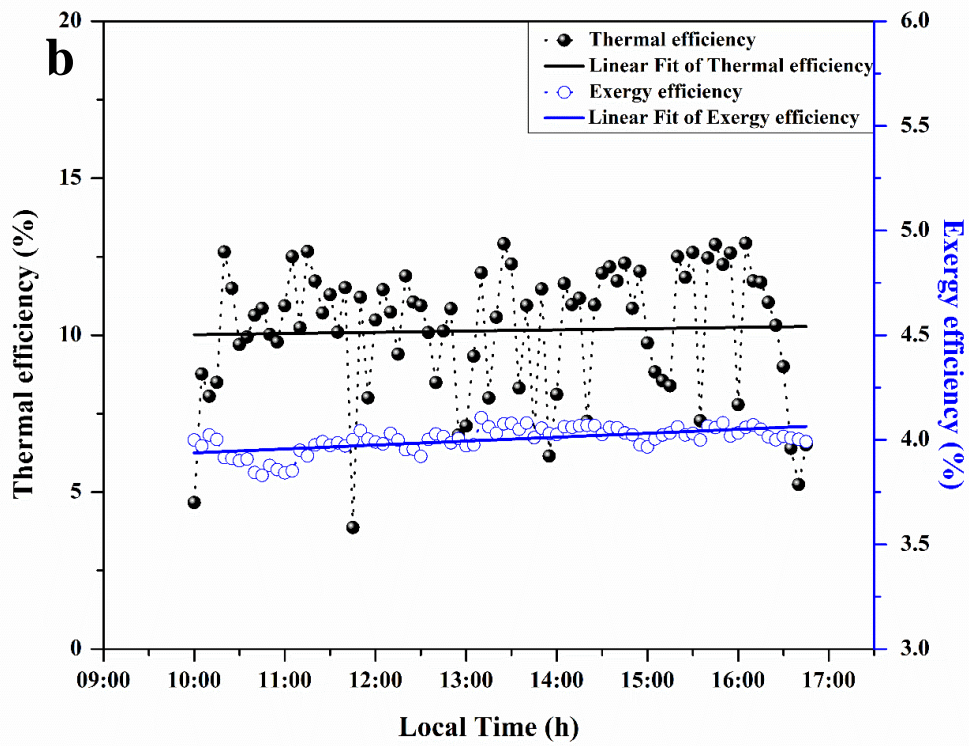


564

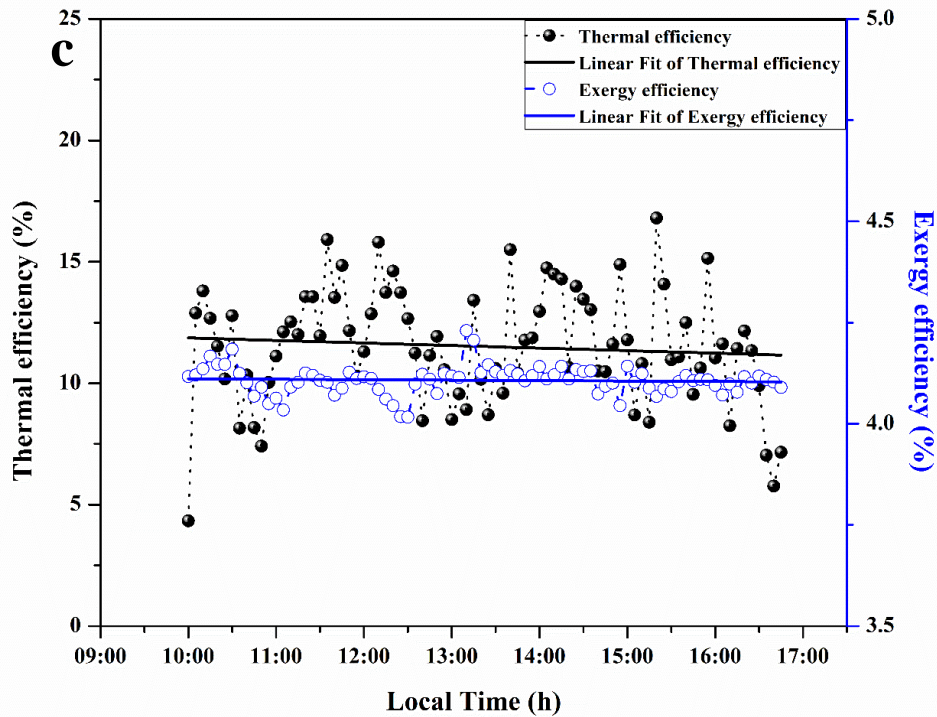
565 **Fig. 20.** (a) Thermal and exergy efficiency of PTDASCC at **0.016 kgs⁻¹**, (b) Variation of thermal
 566 and exergy efficiency with temperature difference (c) Solar radiation data for 18-03-19



567



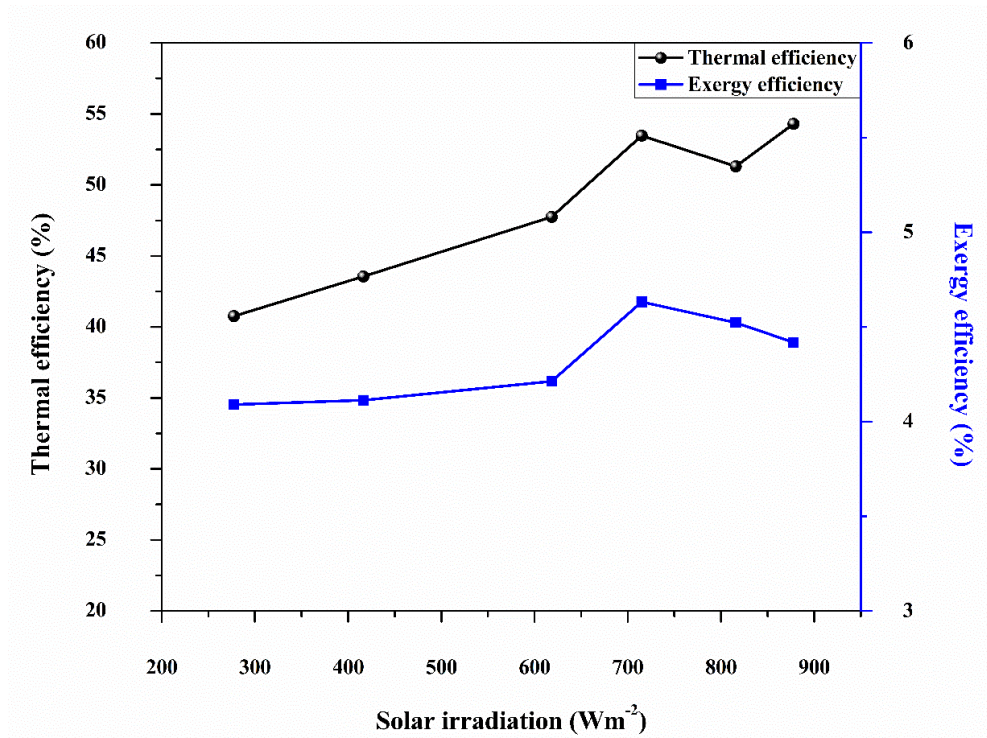
568



569

570 **Fig. 21.** Thermal and exergy efficiency of PTC run with base fluid at (a) 0.016 kgs^{-1} , (b) 0.019
 571 kgs^{-1} and (c) 0.022 kgs^{-1}

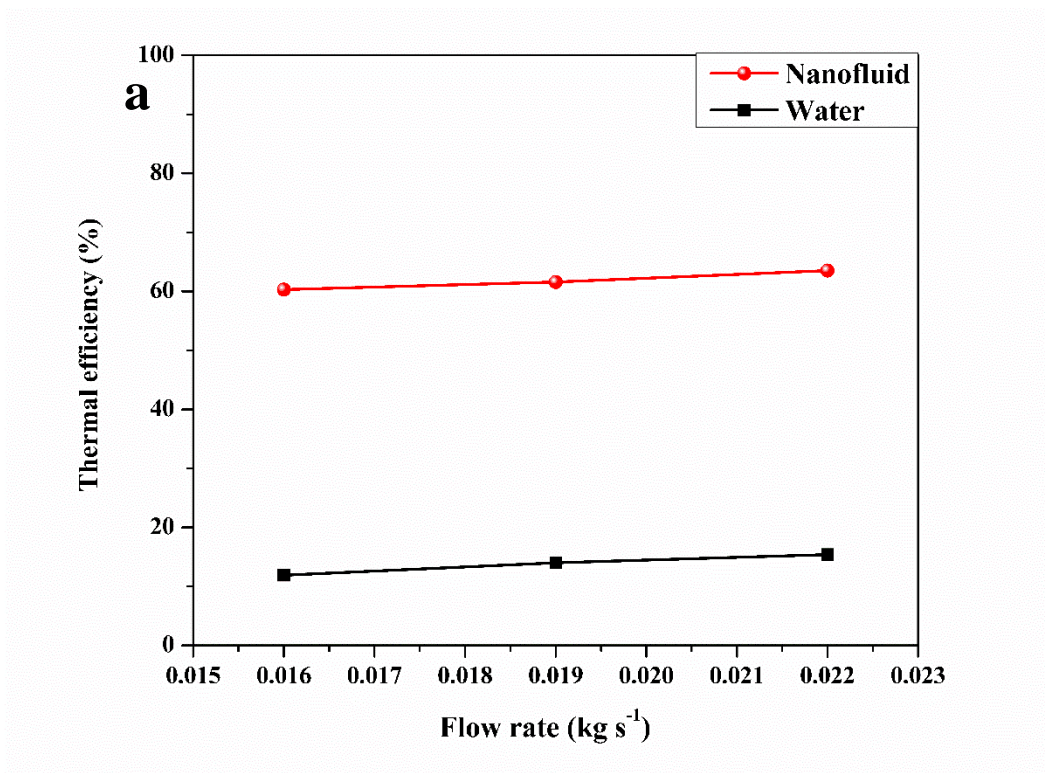
572



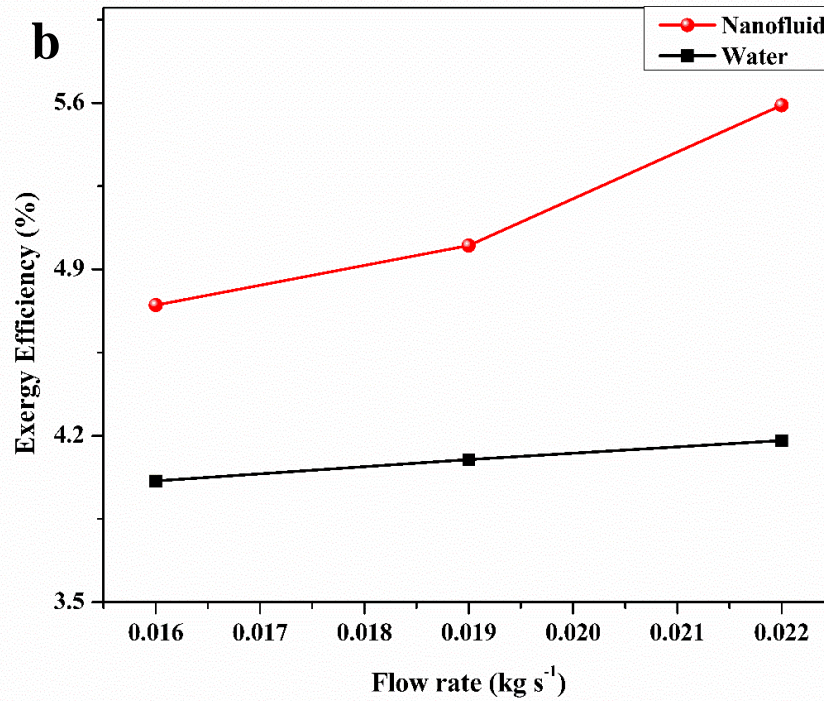
573

574

Fig. 22. Variation of thermal efficiency and exergy efficiency with solar irradiation



575



576

577 **Fig. 23. Variation of (a) thermal efficiency and (b) exergy efficiency with the flow rate**

578 A trendline of thermal and exergy efficiency of the parabolic trough collector at three different
 579 flow rates was generated based on the statistical linear curve fitting technique. The coefficients
 580 and trendline equations of the corresponding curve are given in Table 6. The slope of the line is
 581 represented by ‘b’, while ‘a’ represents the intercept of the fitted line. R² represents the adjacent
 582 R-squared value for each flow rate.

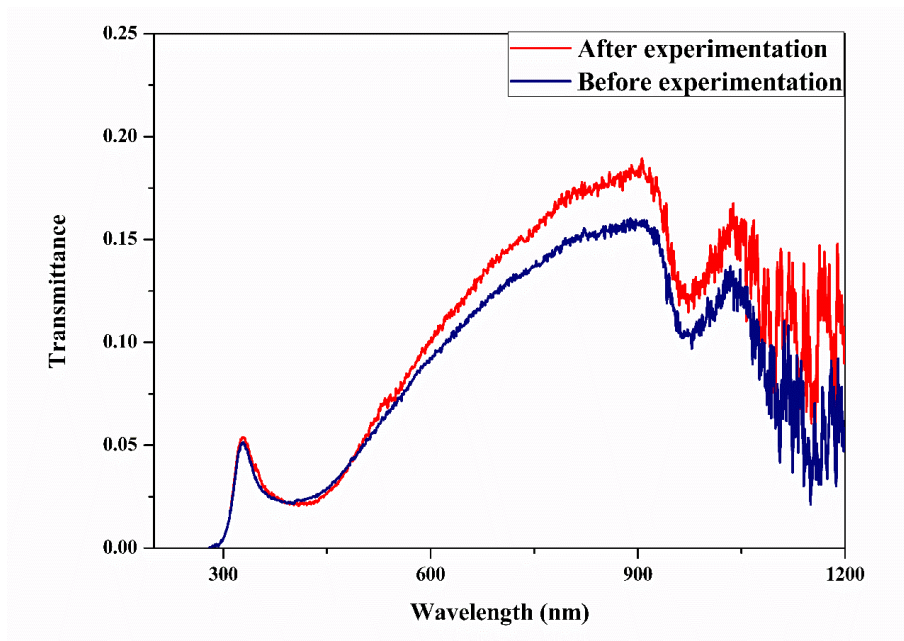
583 **Table 6: Coefficients of efficiency curve at different flow rates**

Working Fluid	Flow rate								
	0.022 kgs ⁻¹			0.019 kgs ⁻¹			0.016 kgs ⁻¹		
Nanofluid	R ²	a	b	R ²	a	b	R ²	a	b
Thermal efficiency	0.587	33.62	0.30	0.675	26.18	3.12	0.573	27.4	2.52
	$\eta_{th} = a + b\Delta T$			$\eta_{th} = a + b\Delta T$			$\eta_{th} = a + b\Delta T$		
Exergy efficiency	0.377	3.89	0.08	0.586	3.48	0.084	0.588	3.45	0.07
	$\eta_{ex} = a + b\Delta T$			$\eta_{ex} = a + b\Delta T$			$\eta_{ex} = a + b\Delta T$		

584 Nanofluid applied solar collectors face the problem of the settling of nanomaterial in the receiver
585 tube. The sedimentation method, as depicted in section 5.4, validates that only a meagre deposition
586 of nanoparticles was observed. In the present system, the nanomaterial which has sedimented on
587 the tube surface after continuous operation for 8 hours was less. An increase in pressure drop due
588 to higher viscosity is a setback associated with the usage of nanofluid [20]. However, the increase
589 in pumping power due to pressure drop was found to be insignificant in the present study. Another
590 issue is the degradation of the optical absorptivity property of nanofluid. Analysis of the
591 retainability of nanofluid's optical absorption was performed, as given in section 6.5.

592 6.5. Analysis of the degradation rate of solar weighted absorption fraction

593 Spectral absorption analysis was employed to analyze the deterioration of stability of optimized
594 nanofluid after being deployed in the solar collector system. Transmittance spectra of nanofluid,
595 before and after running through the hydraulic cycle, is given in Fig. 29. Solar weighted absorption
596 fraction calculated for nanofluid, before and after circulation in the parabolic trough system was
597 observed to be 89% and 88% respectively. A marginal decrease in nanofluid's solar weighted
598 absorption fraction of 1.12% was observed at the end of experimentation. It is concluded that the
599 optimized concentration is not undergoing any degradation in performance due to stability or other
600 issues even after circulating through the hydraulic loop.



601
602 **Fig. 24.** Spectroscopic analysis of optimized nanofluid before and after experimentation in the
603 solar collector

604 7. Conclusions

605 The synthesis and characterization of visible and NIR spectrum absorption concentrated ATO/Ag
606 hybrid nanoparticles have been performed. TEM analysis shows the morphology of silver
607 nanoparticles attached to the surface of ATO nanoparticles. XRD analysis was performed and
608 phase characterization of the hybrid nanoparticle is done. SEM-EDAX and XRD confirm the
609 presence of as stated components in the hybrid nanoparticle. RSM using Central Composite Design
610 produced a minimum of 13 sets of experimental runs. Model prediction of solar weighted
611 absorption fraction is in agreement with the actual data obtained. The relative error between the
612 actual and the predicted value being very less validates the model predictability. Solar weighted
613 absorptivity is observed to be linearly dependent on nanoparticle concentration. The maximum
614 solar weighted absorptivity of 98.90% is obtained at 0.2% ATO/Ag and 0.15% SDS. The
615 optimization of concentrations of nanoparticle and surfactant was performed based on the
616 calculated solar weighted absorptivity of each run. Parametric investigation of the effect of
617 penetration depth on solar weighted absorption fraction and mass fraction on the extinction
618 coefficient was performed. Solar weighted absorption fraction was found to increase exponentially
619 with penetration depth. The extinction coefficient increased linearly with the mass fraction.
620 Investigations on direct absorption parabolic trough solar collectors yielded an optical efficiency
621 of 75% while using ATO/Ag nanofluid. Energy and exergy efficiency were found to be a linear
622 function of the mass flow rate. The highest thermal efficiency obtained for ATO/Ag hybrid
623 nanofluid in PTDASC was 63.5 %. The exergy efficiency of 5.6 % indicates the need to reduce
624 heat loss. The temperature difference across the receiver length decreased with an increase in flow
625 rate. 25% rise in temperature difference was reported on changing flow rate from 0.022 kgs⁻¹ to
626 0.016 kgs⁻¹. It could be concluded from the obtained results, that as the flow rate increases, heat
627 loss is reduced, thereby increasing the energy and exergy efficiency.

628 References

- [1] R.A. Taylor, P.E. Phelan, T.P. Otanicar, C.A. Walker, M. Nguyen, S. Trimble, R. Prasher, Applicability of nanofluids in high flux solar collectors, *J. Renew. Sustain. Energy* 3 (2) (2011) 023104. <https://doi.org/10.1063/1.3571565>.
- [2] J.E. Minardi, H.N. Chuang, Performance of a black liquid flat-plate solar collector, *Sol.*

- Energy 17 (1975) 179-183. [https://doi.org/10.1016/0038-092X\(75\)90057-2](https://doi.org/10.1016/0038-092X(75)90057-2).
- [3] H. Tyagi, P.E. Phelan, R. Prasher, Predicted efficiency of a low-temperature nanofluid-based direct absorption solar collector, *J. Sol. Energy Eng.* 131 (2009) 041004. <https://doi.org/10.1115/1.3197562>.
- [4] T.P. Otanicar, P.E. Phelan, J. S. Golden, Optical properties of liquids for direct absorption solar thermal energy systems, *Sol. Energy* 83 (2009) 969–977. <https://doi.org/10.1016/j.solener.2008.12.009>.
- [5] M. Chen, Y. He, J. Huang, J. Zhu, Investigation into Au nanofluids for solar photothermal conversion, *Int. J. Heat Mass Transf.* 108 (2017) 1894–1900. <https://doi.org/10.1016/j.ijheatmasstransfer.2017.01.005>.
- [6] C.L.L. Beicker, M. Amjad, Enio P. Bandarra Filho, Dongsheng Wen, Experimental study of photothermal conversion using gold/water and MWCNT/water nanofluids, *Sol. Energy Mater. Sol. Cells* 188 (2018) 51–65. <https://doi.org/10.1016/j.solmat.2018.08.013>.
- [7] M. Amjad, H. Jin, X. Du, D. Wen, Experimental photothermal performance of nanofluids under concentrated solar flux, *Sol. Energy Mater. Sol. Cells* 182 (2018) 255–262. <https://doi.org/10.1016/j.solmat.2018.03.044>.
- [8] A.S. Abdelrazika, F.A. Al-Sulaimana, R. Saidur, Optical behavior of a water/silver nanofluid and their influence on the performance of a photovoltaic-thermal collector, *Sol. Energy Mater. Sol. Cells* 201 (2019) 110054. <https://doi.org/10.1016/j.solmat.2019.110054>
- [9] M. Valizade, M.M. Heyhat, M. Maerefat, Experimental comparison of optical properties of nanofluid and metal foam for using in direct absorption solar collectors, *Sol. Energy Mater. Sol. Cells* 195 (2019) 71–80. <https://doi.org/10.1016/j.solmat.2019.01.050>.
- [10] N. Chen, H. Ma, Y. Li, J. Cheng, C. Zhang, D. Wu, H. Zhu, Complementary optical absorption and enhanced solar thermal conversion of CuO-ATO nanofluids, *Sol. Energy Mater. Sol. Cells* 162 (2017) 83–92. <https://doi.org/10.1016/j.solmat.2016.12.049>.
- [11] F. Yu, Y. Chen, X. Liang, J. Xu, C. Lee, Q. Liang, P. Tao, T. Deng, Dispersion stability of thermal nanofluids, *Prog. Nat. Sci. Mater. Int.* 27 (2017) 531-542. <https://doi.org/10.1016/j.pnsc.2017.08.010>.
- [12] X. Yu, Y. Xuan, Investigation on thermo-optical properties of CuO/Ag plasmonic nanofluids, *Sol. Energy* 160 (2018) 200–207.

<https://doi.org/10.1016/j.solener.2017.12.007>.

- [13] Q. Jiang, W. Zeng, C. Zhang, Z. Meng, J. Wu, Q. Zhu, D. Wu, H. Zhu, Broadband absorption and enhanced photothermal conversion property of octopod-like Ag@Ag₂S core@shell structures with gradually varying shell thickness, *Nature* 7 (2017) 17782. <https://doi.org/10.1038/s41598-017-18220-1>.
- [14] J. Zeng, Y. Xuan, H. Duan, Tin-silica-silver composite nanoparticles for medium-to-high temperature volumetric absorption solar collectors, *Sol. Energy Mater. Sol. Cells* 157 (2016) 930–936. <https://doi.org/10.1016/j.solmat.2016.08.012>.
- [15] J. Zeng, Y. Xuan, Enhanced solar thermal conversion and thermal conduction of MWCNT-SiO₂/Ag binary nanofluids, *Appl. Energy* 212 (2018) 809–819. <https://doi.org/10.1016/j.apenergy.2017.12.083>.
- [16] J. Zeng, Y. Xuan, Tunable Full-Spectrum Photo-thermal Conversion Features of Magnetic-Plasmonic Fe₃O₄/TiN Nanofluid, *NANO ENERGY* 2855 (18) 30522-6. <https://doi.org/10.1016/j.nanoen.2018.07.034>.
- [17] A. Joseph, S. Mohan, C.S. Sujith Kumar, A. Mathew, S. Thomas, B.R. Vishnu, S.P. Sivapirakasam, An experimental investigation on pool boiling heat transfer enhancement using sol-gel derived nano-CuO porous coating, *Exp. Therm. Fluid Sci.* 103 (2019) 37–50. <https://doi.org/10.1016/j.expthermflusci.2018.12.033>.
- [18] M. Hemmat Esfe, M. Firouzi, H. Rostamian, M. Afrand, Prediction and optimization of thermophysical properties of stabilized Al₂O₃/antifreeze nanofluids using response surface methodology, *J. Mol. Liq.* 261 (2018) 14–20 <https://doi.org/10.1016/j.molliq.2018.03.063>.
- [19] T.P. Otanicar, Direct absorption solar thermal collectors utilizing liquid-nanoparticle suspensions. Doctor of Philosophy, Arizona State University; 2009.
- [20] A.A. Minea, W. M. El-Maghlany, Influence of hybrid nanofluids on the performance of parabolic trough collectors in solar thermal systems: Recent findings and numerical comparison, *Renew. Energy* 1481 (17) 31297-1. <https://doi.org/10.1016/j.renene.2017.12.093>.

- [21] E. Bellos, C. Tzivanidis, Thermal analysis of parabolic trough collector operating with mono and hybrid nanofluids, *Sustain. Energy Technol. Assess.* <https://doi.org/10.1016/j.seta.2017.10.005>.
- [22] S. Delfani, M. Karami, M.A. Akhavan-Bahabadi, Performance characteristics of a residential-type direct absorption solar collector using MWCNT nanofluid, *Renew. Energy* 87 (2016) 754–764. <https://doi.org/10.1016/j.renene.2015.11.004>.
- [23] M. Vakili, S. M. Hosseinalipour, S. Delfani, S. Khosrojerdi, and M. Karami, Experimental investigation of graphene nanoplatelets nanofluid-based volumetric solar collector for domestic hot water systems, *Sol. Energy* 131 (2016) 119–130. <https://doi.org/10.1016/j.solener.2016.02.034>.
- [24] A. Menbari, A.A. Alemrajabi, A. Rezaei, Heat transfer analysis and the effect of CuO/Water nanofluid on direct absorption concentrating solar collector, *Appl. Therm. Eng.* 104 (2016) 176–183. <https://doi.org/10.1016/j.applthermaleng.2016.05.064>.
- [25] A. Menbari, A.A. Alemrajabi, A. Rezaei, Experimental investigation of thermal performance for direct absorption solar parabolic trough collector (DASPTC) based on binary nanofluids, *Exp. Therm. Fluid Sci.* 80 (2017) 218–227. <https://doi.org/10.1016/j.expthermflusci.2016.08.023>.
- [26] S.A. Kalogirou, S. Karellas, V. Badescu, K. Braimakis, Exergy analysis on solar thermal systems: A better understanding of their sustainability. *Renew Energy* 85 (2016) 1328–33. <https://doi.org/10.1016/j.renene.2015.05.037>.
- [27] T.B. Gorji, A.A. Ranjbar, Thermal and exergy optimization of a nanofluid-based direct absorption solar collector, *Renew. Energy* 106 (2017) 274–287. <https://doi.org/10.1016/j.renene.2017.01.031>.
- [28] M. Karami, Experimental investigation of first and second laws in a direct absorption solar collector using hybrid Fe₃O₄/SiO₂ nanofluid, *J Therm Anal Calorim* 136 (2019) 661–667. <https://doi.org/10.1007/s10973-018-7624-x>.
- [29] Z. Zhang, Y. Ma, X. Bu, Q. Wu, Z. Hang, Z. Dong, X. Wu, Facile one-step synthesis of TiO₂/Ag/SnO₂ ternary heterostructures with enhanced visible light photocatalytic activity, *Nature* 8 (2018)10532. <https://doi.org/10.1038/s41598-018-28832-w>.

- [30] M. Kosmulski, Isoelectric points and points of zero charge of metal (hydr)oxides: 50 years after Parks' review, *Adv. Colloid Interface Sci.* 238 (2016) 1–61. <https://doi.org/10.1016/j.cis.2016.10.005>.
- [31] A. R. Mallah, S. N. Kazi, M. N. M. Zubir, A. Badarudin, Blended morphologies of plasmonic nanofluids for direct absorption applications, *Appl. Energy* 229 (2018) 505–521. <https://doi.org/10.1016/j.apenergy.2018.07.113>.
- [32] W.D. Drotning, Optical properties of solar-absorbing oxide particles suspended in a molten salt heat transfer fluid, *Sol. Energy* 20 (1978) 313–319. [https://doi.org/10.1016/0038-092X\(78\)90123-8](https://doi.org/10.1016/0038-092X(78)90123-8).
- [33] ASTM G173-03, Standard Tables for Reference Solar Spectral Irradiances: Direct Normal and Hemispherical on 37 Tilted Surface, ASTM International, West Conshohocken, 2012.
- [34] P.D. Nasab, A.R. Kelishami, J. Safdari, H. Abolghasemi, Application of emulsion nanofluids membrane for the extraction of gadolinium using response surface methodology, *J. Mol. Liq.* 244 (2017) 368–373. <http://dx.doi.org/10.1016/j.molliq.2017.08.127>.
- [35] X. Lei, J. Shuang, P. Yang, Y. Liu, Parametric study and optimization of dimpled tubes based on Response Surface Methodology and desirability approach, *Int. J. Heat Mass Transf.* 142 (2019) 118453. <https://doi.org/10.1016/j.ijheatmasstransfer.2019.118453>.
- [36] M.U. Sajid, H. M. Ali, Thermal conductivity of hybrid nanofluids: A critical review, *Int. J. Heat Mass Transf.* 126 (2018) 211–234. <https://doi.org/10.1016/j.ijheatmasstransfer.2018.05.021>.
- [37] M.S. Bretado de los Rios, C.I. Rivera-Solorio, A.J. García-Cuellar, Thermal performance of a parabolic trough linear collector using Al₂O₃/H₂O nanofluids, *Renew. Energy* 122 (2018) 665–673. <https://doi.org/10.1016/j.renene.2018.01.094>
- [38] A. Kasaeian, S. Daviran, R. D. Azarian, A. Rashidi, Performance evaluation and nanofluid using capability study of a solar parabolic trough collector, *J. Clean. Prod.* 89 (2015) 368–375. <https://doi.org/10.1016/j.enconman.2014.09.056>.
- [39] ASHRAE Standard 93. Method of testing to determine the thermal performance of solar collectors. Atlanta (GA): American Society of Heating, Refrigerating and Air-Conditioning Engineers; 2010.

- [40] R. Petela, Exergy of undiluted thermal radiation, *Sol. Energy* 74 (2003) 469–488. [https://doi.org/10.1016/S0038-092X\(03\)00226-3](https://doi.org/10.1016/S0038-092X(03)00226-3).
- [41] I. Ceylan, A. Ergun, Thermodynamic analysis of a new design of temperature controlled parabolic trough collector, *Energy Convers. Manag.* 74 (2013) 505–510. <https://doi.org/10.1016/j.enconman.2013.07.020>.
- [42] Q. Wang, M. Hu, H. Yang, J. Cao, J. Li, Y. Su, G. Pei, Energetic and exergetic analyses on structural optimized parabolic trough solar receivers in a concentrated solar thermal collector system, *Energy*, 171 (2019) 611-623. <https://doi.org/10.1016/j.energy.2018.12.211>.
- [43] R. J. Moffat, Describing the uncertainties in the experimental results, *Exp. Therm. Fluid Sci.* 1 (1985) 3-17. [https://doi.org/10.1016/0894-1777\(88\)90043-X](https://doi.org/10.1016/0894-1777(88)90043-X).
- [44] M. Chafie, M.F.B. Aissa, A. Guizani, Energetic end exergetic performance of a parabolic trough collector receiver: An experimental study, *J. Clean. Prod.* 171 (2018) 285-296.
- [45] M. Fana, H. Lianga, S. Youa, H. Zhanga, B. Yinb, X. Wu, Applicability analysis of the solar heating system with parabolic trough solar collectors in different regions of China, *Appl. Energy* 221 (2018) 100–111. <https://doi.org/10.1016/j.apenergy.2018.03.137>.